nature neuroscience

Article

https://doi.org/10.1038/s41593-026-02252-w

Dorsoventral hippocampus neural assemblies reactivate during sleep following an aversive experience

Received: 7 May 2025

Accepted: 3 March 2026

Published online: 01 April 2026

Check for updates

Juan Facundo Morici[1,2], Azul Silva[1,2], Izabela Lima-Paiva[1,2], Éléonore Pronier[1,2] & Gabrielle Girardeau[1,2]

The integration of spatial and emotional components into episodic memory relies on coordinated interactions between hippocampal circuits and emotion-processing regions. Although the dorsal hippocampus (dHPC) supports spatial memory consolidation through sharp-wave ripple (SWR)-associated reactivation, it lacks direct connectivity with key emotional centers such as the amygdala. In contrast, the ventral hippocampus (vHPC) is anatomically and functionally embedded within the emotional network. How the dHPC and vHPC coordinate during sleep to support the processing of complex contextual and emotional experiences remains unclear. Here we used simultaneous electrophysiological recordings from the dHPC and vHPC in rats during sleep following a spatial alternation task under aversive or rewarding emotional valence. We show that coordinated SWRs during non-rapid-eye-movement sleep orchestrate assembly reactivation across the dorsoventral hippocampus. Reactivation after the aversive task more closely mirrors the original neural patterns, driven by the increased recruitment of vHPC shock-responsive neurons and enhanced dHPC spatial replay during coordinated SWRs. Our findings identify a mechanism by which the hippocampus may integrate the spatial and emotional dimensions of an experience during sleep, potentially routing information to the broader emotional memory network.

Episodic memory is supported by the hippocampus[1], a heterogeneous brain structure with distinct functional and anatomical properties along its dorsoventral axis[2,3]. The dorsal hippocampus (dHPC) encodes spatial representations of the environment through the activity of place cells, which code for specific locations called place fields[4]. During non-rapid-eye-movement sleep (NREM), these spatial representations are reactivated[5–7], preferentially during fast oscillatory hippocampal events known as 'sharp-wave ripples' (SWRs)[8]. Dorsal SWRs and the associated reactivation support spatial and contextual fear memory consolidation[9–11]. The integration of spatial information with other features of a lived experience, such as its emotional valence, involves a dialogue between the hippocampus and other structures of the emotional network, supported by the formation of cross-structure neural assemblies coordinated by SWRs[12–14]. There are joint reactivations between the hippocampus and the basolateral amygdala[15] following an aversive spatial experience, and the processing of a reward location involves coordination between the dHPC and the ventral tegmental area[16]. Hippocampal spatial representations are modified by the emotional valence of the environment, a process known as remapping[17,18], relying on the basolateral amygdala (BLA)[19]. For historical and technical reasons, these studies have focused exclusively on the dorsal part of the hippocampus. However, the dHPC has no direct anatomical connections with the BLA and only marginal ones with the rest of the emotional network, including the medial prefrontal cortex (mPFC),

[1]Sorbonne Université, CNRS, Inserm, Center of Neuroscience NeuroSU, Paris, France. [2]Sorbonne Université, CNRS, Inserm, Institut de Biologie Paris-Seine, IBPS, Paris, France. e-mail: gabrielle.girardeau@inserm.fr

https://doi.org/10.1038/s41593-026-02252-w

nucleus accumbens and ventral tegmental area[20,21]. This suggests that the inclusion of the dHPC in the emotional network for the integration of spatial and emotional information into complex memories requires an intermediate structure. The ventral hippocampus (vHPC) displays poorer spatial coding properties than the dHPC[3] but plays a stronger role in emotional processing, particularly in anxiety-like behaviors[22–25] and fear processing[26,27]. Unlike the dHPC, the vHPC has strong reciprocal anatomical and functional connections with the emotion-processing network, notably with the BLA[28–30]. The vHPC also displays SWRs, which are modulated by stress[31,32]. A marginal subset of ventral SWRs (vSWRs) are temporally coordinated with dorsal SWRs (dSWRs) in the absence of any prior learning or emotional experience[33]. vSWRs during sleep co-occur with fast oscillations in the BLA and mPFC and support coordinated reactivation between the vHPC and mPFC after fear conditioning[12], but it is yet unclear whether vSWRs are associated with local vHPC[34] and dorsoventral hippocampal reactivation. Here, we hypothesized that during sleep, coordinated dorsoventral SWRs support the reactivation of neuronal assemblies along the dorsoventral axis of the hippocampus to process spatial and emotional information, potentially supporting their routing to structures selectively connected with the vHPC. Because the vHPC and connected emotional structures, such as the BLA, encode both positive and negative emotions[35–37], we designed a behavioral task that allowed us to examine reactivation of a positive or negative experience triggering similar behaviors in the same spatial contexts. We performed simultaneous electrophysiological recording in the dHPC and vHPC in rats undergoing a spatial alternation task under reward or aversive conditions and during the preceding and following sleep epochs. We identified dorsal, ventral and dorsoventral neuronal assemblies in the hippocampus that represent the aversive and reward conditions of the task and investigated whether and how these assemblies differentially reactivate during subsequent NREM sleep and SWRs.

Results

Rats perform spatial alternation under reward and aversive conditions in the same context

To study the influence of emotional valence on dorsoventral hippocampal coordination, we developed a behavioral task in which animals learn a spatial alternation task on a linear track under two motivational contingencies associated with opposite valence. In the reward-motivated condition associated with a positive valence, the rats run back and forth on the linear track to obtain a small water reward at the end of each lap ('reward run'). The aversion-motivated condition, associated with a negative valence, was conducted on the same linear track and signaled by a single, constant light cue. Under this condition, animals run back and forth to avoid an eyelid shock ('aversive run') delivered after 20–30 seconds of immobility (Fig. 1). The animals were first pretrained to alternate sides in the reward condition. The aversive condition was then gradually introduced to preserve the mobility and alternation behavior (Extended Data Fig. 1a). The recordings started at plateau performance for both the reward and shock conditions. Because the animals rapidly reach stable performance in the reward condition, plateau performance was defined as a drop in the number of shocks by at least 50% (Fig. 1b, bottom). The number of reward laps and the number of aversive laps and shocks remained stable across all subsequent recording sessions (Fig. 1b, top and center; a lap is defined as one left-to-right or right-to-left run). Each recording day started with a baseline sleep and rest session in the homecage (sleep 1), followed by the aversive run and a second sleep session in the homecage (sleep 2). The animals then performed the reward run before the final sleep session in the homecage (sleep 3; Fig. 1a). The homecage sessions lasted 2–3 hours, and the order of the reward and aversive conditions was switched every day. Animals explored homogeneously the linear track in both aversive and reward conditions (Extended Data Fig. 1b). The speed was globally lower in aversive laps compared to reward ones (Extended Data Fig. 1c), but the

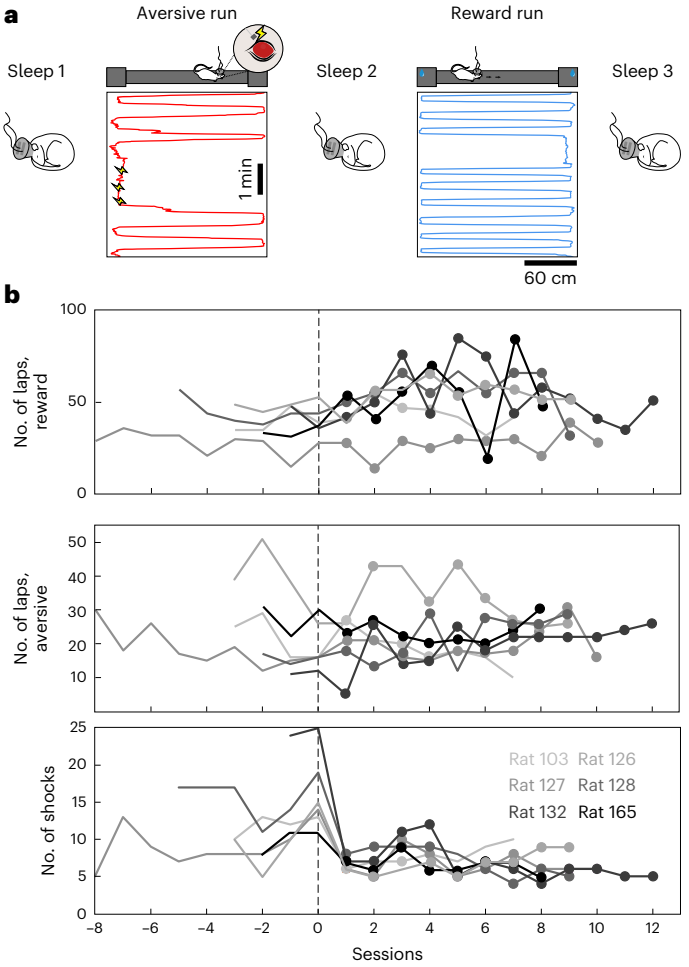

Fig. 1 | Rats perform aversive and reward-motivated alternation on a linear track. a, Example trajectories while rats run back and forth on a linear track to avoid eyelid shocks (aversive run, red; yellow lightning indicates the shocks) or to receive a water drop (reward run, blue). Before and after each run, animals were allowed to sleep in their homecage (sleep 1–3). **b**, Number of reward laps, aversive laps and shocks during pretraining (−8 to 0) and during recording days (1–12) at plateau performance starting as a 50% drop in the number of shocks received. Full dots indicate the recording days included in the analysis ($N_{Sessions}$ = 47).

speed distributions across space were similar (Extended Data Fig. 2a). To control for behavioral differences across conditions, we used a speed threshold to divide the time on the linear track into active or quiet states. We did not find significant differences in occupancy in either of these states across space (Extended Data Fig. 2b,c) or in total time between conditions (Extended Data Fig. 1d). Subsequent neural analysis were restricted to active states, except for a control using quiet states.

Population and spatial coding in the vHPC better disambiguate the reward and aversive conditions

We recorded local field potentials (LFPs) and neuronal ensembles from the dorsal and ventral CA1 hippocampal regions with custom and commercial electrodes (Fig. 2a,b and Supplementary Fig. 1) across a total of 47 recording days in six female Long–Evans rats. Each unit was classified as putative pyramidal cell (Pyr) or interneuron (Int) based on the spike waveform (Methods and Extended Data Fig. 3a–d). In total, we identified 1,615 units (dHPC, 22.79 ± 2.22; vHPC, 11.57 ± 1.96; mean ± s.e.m. units per session) across both regions: 544 units from the vHPC (Pyr, 461; Int, 83) and 1,071 from the dHPC (Pyr, 856; Int, 215). As expected, the firing rate was higher in putative interneurons compared to putative pyramidal cells in both regions, and putative pyramidal cells in the

https://doi.org/10.1038/s41593-026-02252-w

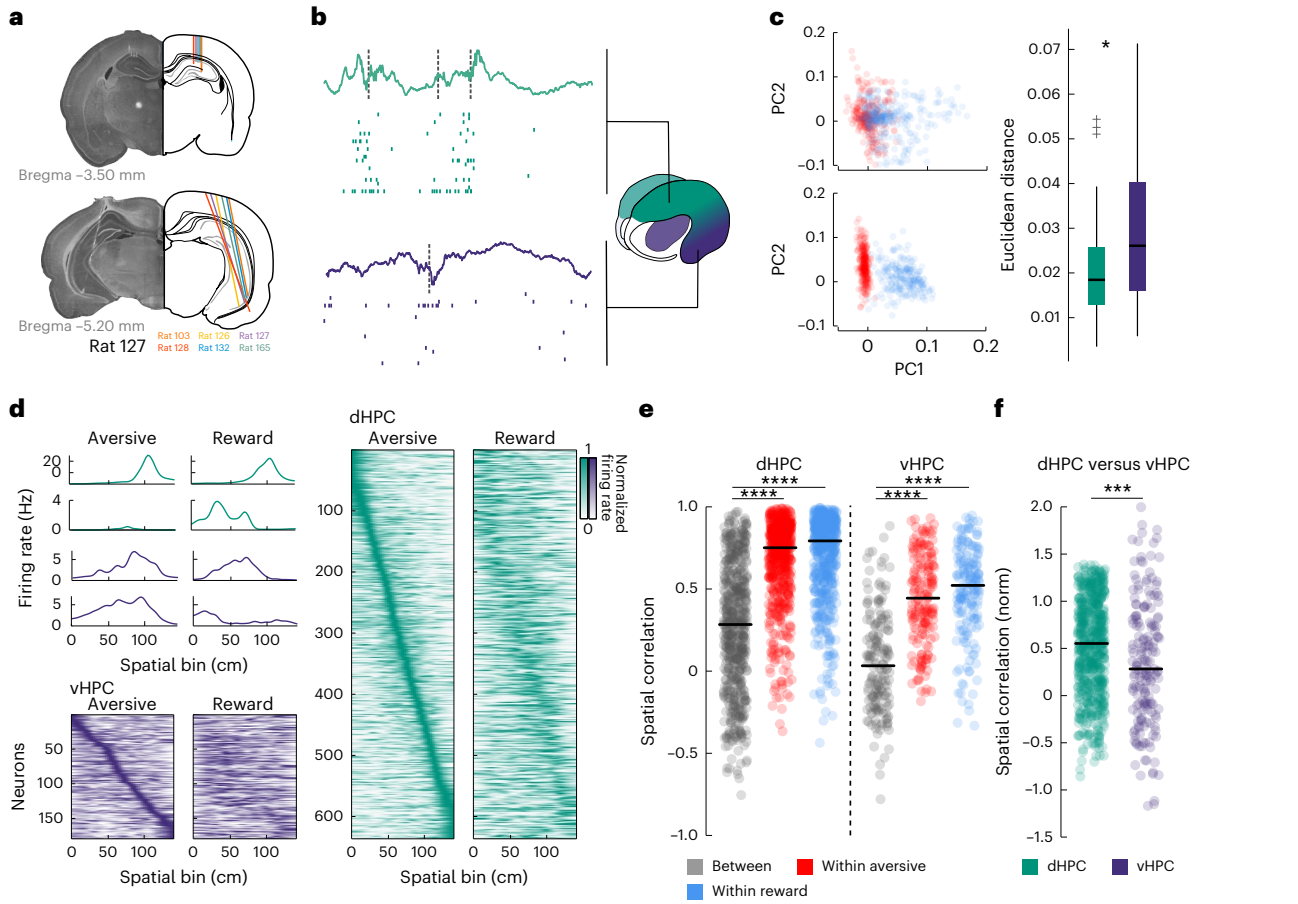

Fig. 2 | vHPC population activity and spatial coding better distinguish aversive from reward sessions. a, Histological reconstruction of electrode placement in the dHPC and vHPC for all animals (one color per rat). **b**, Example LFP and spiking activity from the dHPC (green) and vHPC (purple) during NREM sleep. Dotted lines indicate SWRs. **c**, Left: example of PCA-projected population spiking activity during exploration behavior in the reward (blue) and aversive (red) runs for the dorsal (top) and ventral (bottom) single units for one recording session. Right: comparison of Euclidean distance between centroids of reward and aversive PCA-projected clouds obtained with the dorsal and ventral hippocampal population activity for all recording sessions (two-sided Mann–Whitney test, $^{*}P = 0.012$; number of sessions, $N_{dorsal} = 37$, $N_{ventral} = 35$; whiskers extend to minimal and maximal data points; box edges are 25th and 75th percentiles; black line, median; grey '+', outliers beyond the whisker limits). **d**, Top left: pyramidal cells identified as place cells in at least one session. Place fields of four example place cells of the dHPC (green) and vHPC (purple) in the aversive and reward conditions. Bottom left and right: all cells identified as place cells in at least one session, sorted according to the position of their peak response during the aversive run in the dHPC (green) and vHPC (purple). **e**, Spatial correlation of tuning curves within reward or aversive sessions and between conditions, for dorsal (left) and ventral (right) place cells (two-sided Friedman test, $^{****}P = 1.88 \times 10^{-137}$; Tukey–Kramer post hoc test, dHPC: $^{****}P_{between\text{-}within\ aversive} = 2.20 \times 10^{-16}$, $^{****}P_{between\text{-}within\ reward} = 2.2 \times 10^{-16}$, $P_{within\ aversive\text{-}within\ reward} = 0.06$; vHPC: $^{****}P_{between\text{-}within\ aversive} = 1.77 \times 10^{-24}$, $^{****}P_{between\text{-}within\ reward} = 2.2 \times 10^{-16}$, $P_{within\ aversive\text{-}within\ reward} = 0.31$; number of single units, $N_{dHPC} = 656$, $N_{vHPC} = 193$; black line, mean). **f**, Normalized spatial correlation between reward and aversive sessions for dorsal (green) and ventral (purple) place cells (two-sided unpaired Wilcoxon test, dHPC versus vHPC, $^{***}P = 0.0003$; number of single units, $N_{dHPC} = 656$, $N_{vHPC} = 193$; black line, mean).

dHPC exhibited a higher burst index than vHPC putative pyramidal cells (Extended Data Fig. 3e,f). First, we analyzed the population-level representation in each hippocampal region during exploratory behavior in both aversive and reward runs. To do so, we applied principal component analysis (PCA) to the multineuronal activity from the dHPC and vHPC during each condition and calculated the Euclidean distance between the centroids of each condition's coefficient cloud projected on PCs 1 and 2. The Euclidean distance between the two conditions was significantly higher for the vHPC compared to the dHPC (Fig. 2c), indicating that the population activity in the vHPC disambiguates the reward and aversive conditions better than the dHPC. Then we characterized place-cell activity across the two regions and conditions. Spatial coding is known to be less precise in the vHPC compared to the dHPC[3,24]. Indeed, place cells made up 52% and 63% of putative pyramidal neurons in the dHPC but only 17% and 29% in the vHPC in the aversive and reward conditions, respectively (Extended Data Fig. 4a). Place fields were larger and peak firing rates lower in the vHPC compared to the dHPC, but neither these parameters nor the spatial information content differed between conditions in the dHPC or vHPC (Extended Data Fig. 4b,c). Finally, we assessed place-cell remapping across conditions. We found that both structures remapped significantly between conditions compared to within conditions (Fig. 2d,e). When normalizing by the average within-session spatial correlation, we found that remapping between conditions was higher in the vHPC than in the dHPC (Fig. 2f). Thus, the degraded spatial code found in the vHPC still contributes to the disambiguation between conditions, suggesting that place cells in the vHPC are more impacted by the change in contingency. Because the spatial context stays the same but the valence differs between conditions, this aligns with the preferential roles of the dHPC and vHPC in spatial and emotional processing, respectively[2,3].

The shock differentially modulates neuronal responses in the dHPC versus vHPC

Both the dHPC and vHPC can respond to aversive stimuli during fear conditioning[26,38,39]. Here, the shock was not associated to a cue or a context but to a specific behavior (immobility), and it was meant to promote

https://doi.org/10.1038/s41593-026-02252-w

a structured avoidance behavior (that is, alternation) in the absence of a defined safe location. This creates a threatening condition in the otherwise stable context. To check for shock responsiveness in our task, we constructed firing curves for putative pyramidal cells in both the dHPC and vHPC (Fig. 3a). We found that a significantly higher proportion of neurons in the dHPC exhibited an increase in their response during the shock (Fig. 3b). However, the shock systematically increased the speed of the animal (Fig. 3c), and speed is known to influence the firing of dorsal and ventral hippocampal neurons, albeit to a different extent: dorsal neurons are more speed-modulated than ventral neurons[40]. In our data, the proportion of speed-modulated neurons within the vHPC shock-responsive neurons was the same as for vHPC non-shock-responsive neurons. In the dHPC, the shock-responsive neurons were slightly enriched in speed-modulated neurons compared to the non-shock-responsive neurons (Extended Data Fig. 5a–c). To account for the bias in shock response due to the increase in speed, we decorrelated speed from the neuronal response (Methods). Although dorsal units exhibited a significant decrease in the magnitude of shock response upon decorrelation, ventral shock-responsive units showed no significant change. Once controlled for speed, the vHPC showed a stronger response to the shock than the dHPC (Fig. 3d,e). Unlike in the dHPC, shock cells in the vHPC do not increase their activity at transitions from quiet to active behavior in the absence of shock. In shock-responsive neurons, the maximal shock response significantly correlated with the magnitude of speed modulation for the dHPC neurons but not for the vHPC neurons. (Extended Data Fig. 5d,e). We also investigated the link between shock cells and place cells. In the dHPC or vHPC, the proportion of shock-responsive neurons is not significantly different among place cells versus non-place cells. The place fields of shock-responsive place cells were not closer to the location of the first shock compared to the place fields of non-shock-responsive place cells, indicating that the shock does not turn nearby place cells into shock-responsive neurons. Dorsal shock-responsive place cells exhibited lower spatial information values than pure place cells, whereas this effect was absent in the vHPC, where spatial information is already significantly lower (Extended Data Fig. 5f–h). In the reward condition, we found a similar proportion of reward-responsive cells in the dHPC and vHPC (Fig. 3f,g). Because the reward is consumed during immobility (Fig. 3h), speed decorrelation does not affect reward responsiveness in either structure, but the responses are higher in the dHPC (Fig. 3i,j). Altogether, these results indicate that both the dHPC and vHPC respond to shock and reward. In the dHPC, shock responsiveness is strongly influenced by speed and, to a lesser extent, space, whereas the vHPC exhibits strong shock responsiveness largely independent of speed and place modulation.

Dorsoventral hippocampal joint assemblies better disambiguate the reward and aversive conditions

Functional communication between structures relies on the formation of neuronal assemblies composed of members distributed across these regions[14,41,42]. We examined whether the dHPC and vHPC could bind spatial and emotional information via the formation of dorsoventral neuronal assemblies. The assemblies were detected during the aversive or the reward condition using a PCA-independent component analysis (ICA) method[43] (Supplementary Fig. 2) on all simultaneously recorded pyramidal neurons in the dHPC and vHPC. The detection was restricted to moments of active behavior (Extended Data Fig. 2c). For each of the 446 detected assemblies, we applied a threshold to the ICA weight vectors to determine the neurons that were significantly contributing to the assembly (Fig. 4a). We differentiated 277 assemblies with only dHPC contributing members (131 aversive and 146 reward), 62 assemblies with only vHPC members (37 aversive and 25 reward) and 107 assemblies with contributing members from both the dHPC and vHPC. We called these assemblies 'joint assemblies' (54 aversive and 53 reward, 23.99% of detected assemblies). We did not detect differences in the number or proportion (Supplementary Fig. 3) of members across assembly types (dorsal, ventral, or joint). Most dorsal and ventral members of joint assemblies were unique to those assemblies, rather than shared with purely region-specific assemblies (aversive dHPC, 66.66%, $N = 120$; reward dHPC, 60.23%; aversive vHPC, 82.66%, $N = 143$; reward vHPC, 88.30%, $N = 166$). To compare the overlap between assemblies detected in either the aversive or the reward condition on the same set of neurons, we computed the similarity index across pairs of dorsal, ventral or joint assemblies and identified the pairs that were significantly similar between the two conditions (Fig. 4b). The percentage of assemblies that overlapped between the two conditions was significantly lower for the joint assemblies compared to the dorsal or ventral assemblies (Fig. 4c). Hence, although the global activity in the vHPC alone disambiguates the valence of the context better than the dHPC (Fig. 2c,f), at the level of assemblies specifically involved in each condition, representations associating both the dHPC and vHPC lead to a better disambiguation of the reward versus aversive experience in the same context.

Dorsal, ventral and joint hippocampal assemblies reactivate during sleep after the reward and aversive conditions

During sleep after an experience, the neural patterns of exploration show an increased activation compared to pre-experience sleep. This reactivation phenomenon occurs within the dHPC[5,7] and between the dHPC and structures related to valence processing[3,15,16,44]. The extent to which reactivation occurs in the vHPC is yet unclear[34], and it is unknown how the vHPC coordinates with the dHPC during sleep following an emotional experience. To address this question, for each joint assembly detected during the aversive or reward experience, we calculated the activation strength during the rest of the recording session, including REM and NREM sleep in the homecage (Fig. 4d). We used a threshold to identify activation peaks and calculated the activation peak rate per minute. This quantitative measure indicates the frequency at which the assembly appears during NREM sleep before and after the reward or aversive exploration (Fig. 5a). Both aversive and reward joint assemblies exhibited higher activation rates

Fig. 3 | Shock responsiveness is higher in the vHPC than in the dHPC. **a**, Normalized perishock responses for all dHPC (left) and vHPC (right) neurons. **b**, Percentage of shock-responsive neurons in the dHPC and vHPC (χ^2, $^*P = 0.03$). **c**, Mean speed centered on shock onset for all aversive sessions in all animals ($N_{sessions} = 47$, $N_{shocks} = 4–13$ per session; shaded area, ±s.e.m.). **d**, Mean *Z*-scored response to shocks for shock-responsive neurons (green/purple) and non-responsive neurons (gray) in the dHPC (top) and vHPC (bottom). When decorrelated from speed (orange), the response of shock-responsive neurons decreases significantly more in the dHPC than in the vHPC (solid lines, mean; shaded areas, ±s.e.m.). **e**, Maximal response during shock for shock-responsive (dHPC/vHPC, green/purple) and shock-responsive decorrelated activity (orange) (paired two-way ANOVA, $P_{structure} = 0.051$, $F = 3.8$, $^{**}P_{speed} = 0.004$, $F = 8.24$, $P_{interaction} = 0.59$, $F = 0.29$; Tukey–Kramer post hoc test with Bonferroni correction, $dHPC_{shock}$ versus $dHPC_{decorr}$: $^{**}P = 0.003$, $dHPC_{decorr}$ versus $vHPC_{decorr}$: $^*P = 0.01$; number of single units, $N_{dHPC} = 277$, $N_{vHPC} = 123$; black line, mean). **f**, Normalized perireward responses for all dHPC (green) and vHPC (purple) neurons. **g**, Percentage of reward-responsive neurons in the dHPC and vHPC (χ^2, $P = 0.36$). **h**, Mean speed centered on reward trigger for all reward sessions in all animals ($N_{sessions} = 47$, $N_{rewards} = 9–86$ per session; shaded area, ±s.e.m.). **i**, Mean *Z*-scored response to valve opening for reward-responsive neurons (dHPC/vHPC, green/purple; corresponding responses decorrelated from speed in orange) and non-responsive neurons (gray) (solid lines, mean; shaded areas, ±s.e.m.). **j**, Maximal response during reward consumption for reward-responsive (dHPC/vHPC, green/purple) and shock-responsive decorrelated activity (orange) (paired two-way ANOVA, $^{****}P_{structure} = 3 \times 10^{-26}$, $F = 120.3$, $P_{speed} = 0.23$, $F = 1.41$, $P_{interaction} = 0.36$, $F = 0.85$; Tukey–Kramer post hoc test with Bonferroni correction, $^{****}P = 2.9 \times 10^{-5}$; number of single units, $N_{dHPC} = 281$, $N_{vHPC} = 140$; black line, mean).

https://doi.org/10.1038/s41593-026-02252-w

during postsleep compared to presleep periods, establishing the existence of joint dorsoventral hippocampal reactivation (Fig. 5b). The presleep-to-postsleep difference diminishes over the course of the sleep session (0–20 min versus 20–40 min of NREM sleep; Fig. 5b), consistent with previous observations that reactivation rapidly declines over the first hour of NREM sleep[12,15]. The same result was observed for dorsal and ventral assemblies (Extended Data Fig. 6). This was not due to concatenating fragmented NREM bouts into a single block (Methods), because the condition did not modify the general structure of the following sleep (REM and NREM bouts, number and durations; Supplementary Figs. 4 and 5), and NREM assembly reactivation also showed a significant decay in real time elapsed from the beginning of the first NREM epoch (Supplementary Fig. 6). No reactivations were found during REM sleep (Extended Data Fig. 7a). Thus, our results show

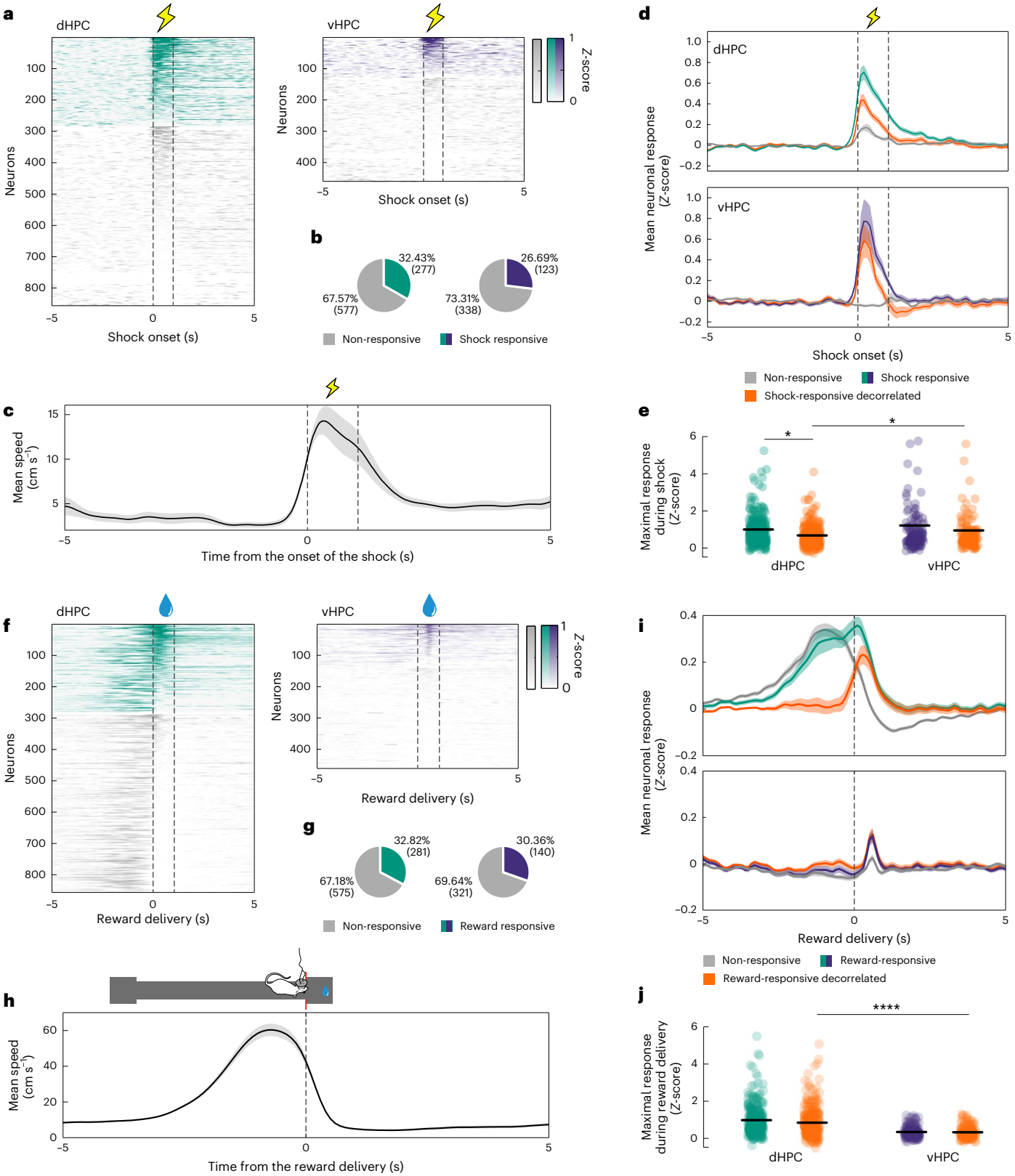

https://doi.org/10.1038/s41593-026-02252-w

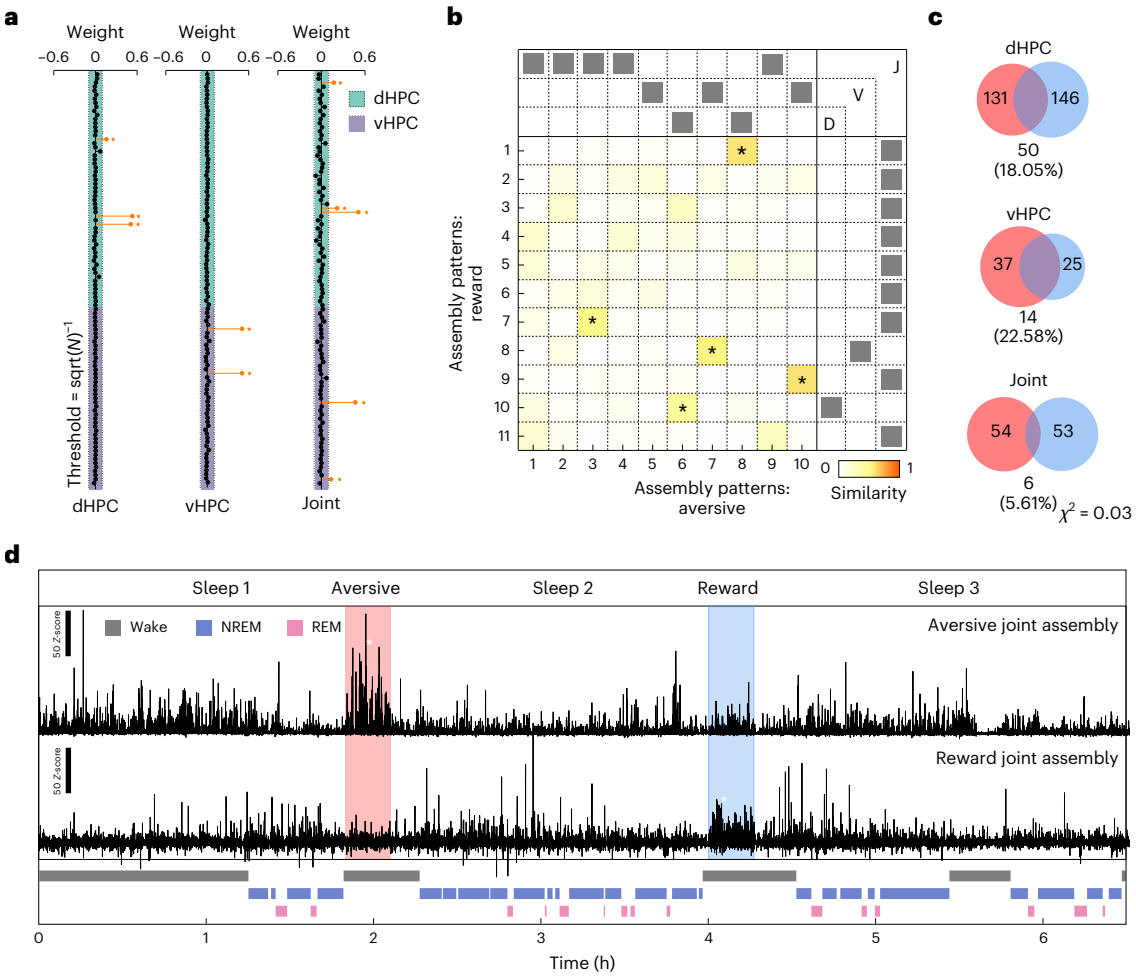

Fig. 4 | Assembly detection during aversive and reward runs. a, Examples of a dHPC (left), vHPC (middle) and joint (right) assembly from a representative session with assembly members (orange lollipops) in the dHPC, vHPC or both, respectively. **b**, Example of an assembly similarity index matrix for dHPC (D), vHPC (V) and joint (J) assemblies. The index was calculated as the dot product of all assembly pairs in the session. Two assemblies were considered significantly similar (*) if the similarity index was above the 99.9 percentile of a surrogate distribution. **c**, Venn diagrams of significantly similar aversive (red) and reward (blue) assemblies for dHPC (top), vHPC (middle) and joint (bottom) assemblies. Joint assemblies showed the lowest overlap between conditions (χ^2, $^*P = 0.03$). **d**, Examples of assembly activity strength during the whole recording session for a joint aversive assembly (red) and a joint reward assembly (blue).

that NREM sleep reactivation after an emotional experience extends beyond the dHPC and includes reactivation in the vHPC as well as coordinated reactivation across the full hippocampal axis after both reward and aversive experiences.

Aversive joint assemblies reflect more accurately the awake experience

Next, we investigated potential differences between the joint dorsoventral assembly reactivation after a reward versus an aversive experience. We calculated the average activation strength across peaks during NREM sleep before and after exploration. This qualitative measure reflects the similarity in coactivation patterns of members between the assemblies activated during NREM sleep and the 'original' assemblies detected during the aversive or reward experience. Then we computed the presleep-to-postsleep ratio between these values to obtain the peak reactivation strength (Methods). A positive peak reactivation strength indicates that assemblies activated in sleep after the experience show a higher fidelity to the experience assemblies compared to assemblies in sleep preceding it. We observed that the peak reactivation strength was significantly different from zero for the joint aversive assemblies but not for the reward joint assemblies (Fig. 5c) and not for the aversive or reward dHPC or vHPC assemblies (Extended Data Fig. 8a). The peak reactivation strength was not different from zero for any assembly type during REM sleep (Extended Data Fig. 7b). Thus, when reactivated during post-experience NREM sleep, the joint aversive assemblies are more similar to the original assemblies that emerged during the aversive experience compared to pre-experience NREM assemblies. Finally, we found that the peak reactivation strength of joint aversive assemblies correlated positively with the activation strength of the assemblies during the exploration of the aversive condition (Fig. 5d). This correlation was selective for joint aversive assemblies and not significant for either joint reward assemblies or dHPC/vHPC assemblies in either condition (Fig. 5d and Extended Data Fig. 8b). This indicates that the increase in peak activation strength of the aversive joint assemblies during NREM sleep was initiated during the preceding exploration of the track. Indeed, joint-assembly peak reactivation strength showed a positive correlation with the percentage of active exploration during aversive run sessions, but not in the reward condition, where movement itself has no behavioral relevance. Peak reactivation strength was not influenced by the number of shocks or rewards (Supplementary Fig. 7). This suggests that behavioral engagement in the aversive session—where animals avoided shocks by actively moving through space—influenced the strength of reactivation during subsequent sleep. Altogether, our results show that spatial exploration under reward or aversive conditions recruits assemblies spanning both the dHPC and vHPC.

https://doi.org/10.1038/s41593-026-02252-w

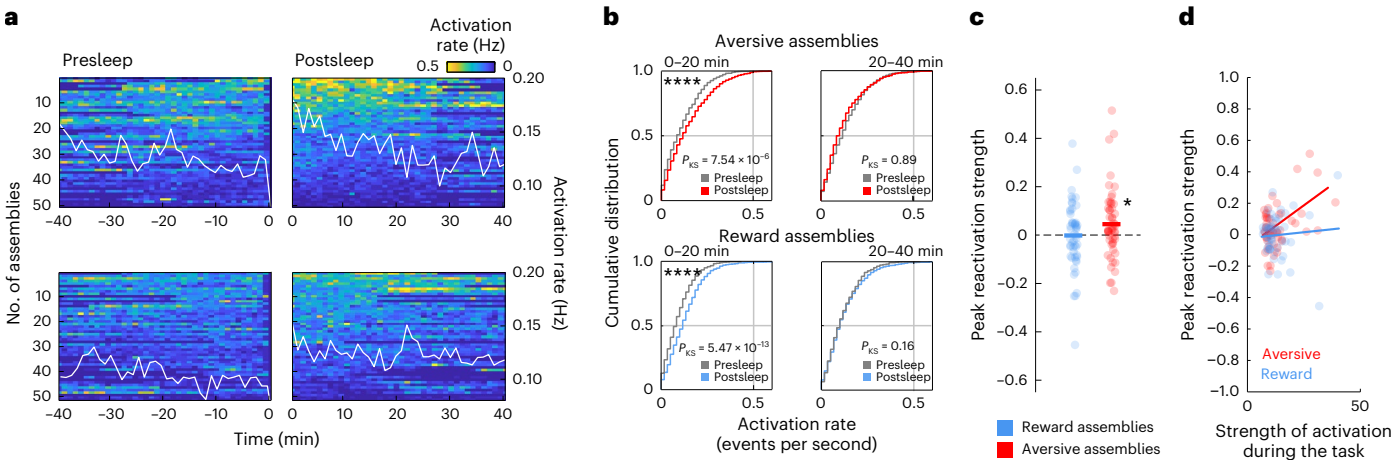

Fig. 5 | Joint assembly reactivation during NREM sleep. a, Assembly peak activation rate across time during presleep and postsleep sessions for all aversive (top) and reward (bottom) assemblies (number of assemblies, $N_{Aversive} = 50$, $N_{Reward} = 51$). **b**, Cumulative distributions of peak activation rates including presleep (in gray) and postsleep reactivation rates for aversive (red) and reward (blue) assemblies. Note the significant increase in activation rate in postsleep versus presleep for both types of assemblies in the first 20 minutes of NREM sleep (two-sided Kolmogórov–Smirnov test, $^{****}P < 0.0001$). **c**, Peak reactivation strength for aversive and reward assemblies, significantly different from zero for aversive joint assemblies only (one-sided Mann–Whitney test against zero, $^{*}P = 0.014$; Mann–Whitney test, $P = 0.08$; number of assemblies, $N_{Aversive} = 54$, $N_{Reward} = 53$). **d**, Joint aversive assemblies' reactivation strength correlates with their activation during the task (linear regression; aversive, $R^2 = 0.22$, $^{**}P_{slope} = 0.0004$; reward, $R^2 = 0.017$, $P_{slope} = 0.35$; number of assemblies, $N_{Aversive} = 52$, $N_{Reward} = 53$).

These assemblies will be later reactivated during NREM sleep, with joint aversive assemblies showing a strong fidelity to the assemblies that emerged during the experience.

Coordinated SWRs following the aversive condition are associated with increased dorsal sequence replay

Dorsal HPC reactivations have consistently been found to co-occur with SWRs[45]. SWRs were shown to mediate the synchronization of the dHPC activity with distant structures[13,15,16]. Although a subset of SWRs coordinate between the dHPC and vHPC during baseline NREM sleep[33], it is yet unknown how spatial exploration associated with an emotional valence affects vHPC SWRs and their coordination with dHPC SWRs during subsequent sleep. To detect SWRs in the dorsal (dSWRs) and ventral (vSWRs) hippocampus, we used the oscillatory component (ripple) of the SWRs by thresholding the normalized square root of the filtered LFP recorded in the CA1 pyramidal layer (Fig. 6a,b). As previously established, we found that dSWR rates were significantly higher than vSWR rates[33] (Fig. 6c). However, the vSWR rate did not increase during sleep following either the reward or the aversive session, unlike the dSWR rate (Supplementary Fig. 8a). Ripples tend to occur in bursts, as shown by the shape of the autocorrelograms (Supplementary Fig. 8b). We did not observe changes in the 'burstiness', amplitude or duration of dSWRs or vSWRs after the aversive or reward experience (Supplementary Fig. 8c–e).

Next, we explored the fine temporal coordination between dorsal and ventral ripples. On the cross-correlation between dorsal and ventral ripples, the central peak was shifted to positive time bins, suggesting that vSWRs tend to occur after dSWRs (Extended Data Fig. 9a). We defined coordinated events as events during which a vSWR occurred within ±100 ms of a dorsal one. Both dorsal and ventral ripples showed a percentage of coordinated events significantly higher than chance (Fig. 6d; median: dHPC, 16.83%; vHPC, 19,81%). Surprisingly, neither the proportion of coordinated events nor their directionality (dHPC versus vHPC leading) changed after either the reward or the aversive condition compared to baseline (Extended Data Fig. 9b–d), suggesting that changes in coordination occur at a finer scale. The amplitude of coordinated dorsal and ventral ripples was higher than the amplitude of uncoordinated ripples (Extended Data Fig. 9e), as reported previously[33], and coordinated ripples occur more in bursts than uncoordinated ones (Fig. 6e,f). The recruitment of single dHPC and vHPC units by dorsal or ventral ripples, respectively, does not differ between coordinated and uncoordinated ripples (Extended Data Fig. 9f–h). Dorsal neurons and ventral neurons do not respond to uncoordinated vSWRs and dSWRs, respectively, but both dorsal and ventral neurons respond during coordinated SWRs of the opposite pole (Fig. 6g). This suggests that coordinated events represent a privileged time window for cross-hippocampal neuronal communication. Dorsal ripples are known to support the reactivation of spatial sequences[5,6]. Because we hypothesized that coordinated events provide a time window in which dorsal spatial information and ventral emotional information are jointly engaged, we investigated whether the spatial content in the dHPC differed between coordinated and uncoordinated SWRs. We detected sequence replay using a Bayesian decoding method and found that 8.81 ± 0.63% of dorsal ripples contained significant replay events[46]. We then separated significant replay events occurring during coordinated versus uncoordinated SWRs. The percentage of significant replay was significantly increased during coordinated SWRs following the aversive condition, but not the reward condition (Fig. 6h). These results were replicated using rank-order correlation as an alternative detection method (Supplementary Fig. 9). Together, these results indicate that coordinated SWRs are enriched in relevant spatial content after an aversive experience.

Coordinated SWRs support stronger joint aversive assembly reactivation through increased recruitment of vHPC shock-responsive neurons

We hypothesized that coordinated dorsoventral SWRs support the reactivation of joint assemblies. We showed that the peak reactivation strength for joint aversive assemblies is significantly different from zero and significantly different from the peak reactivation strength of reward assemblies during coordinated SWRs, but not during uncoordinated SWRs (Fig. 7a). This effect was not due to merging uncoordinated vSWRs and dSWRs (Supplementary Fig. 10) and was specific to joint assemblies (Supplementary Fig. 11a,b). To rule out the possibility that the absence of increased peak activation for reward joint assemblies was due to excluding quiet awake periods—when reward consumption and synchronous activity could

https://doi.org/10.1038/s41593-026-02252-w

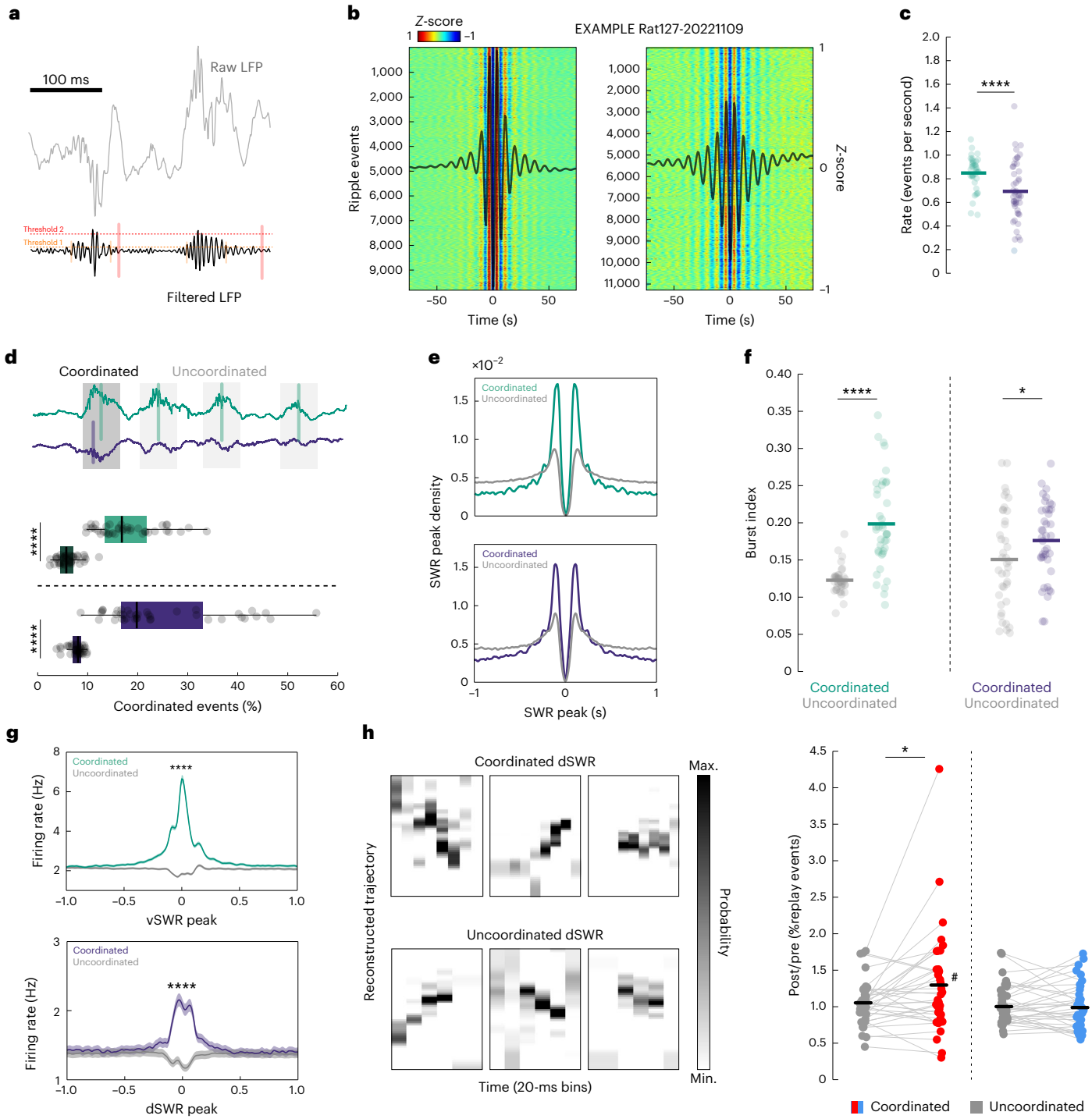

Fig. 6 | Ripple coordination across dorsoventral hippocampal axis preferentially sustains replay of spatial sequences. a, Example raw and filtered LFP of the dHPC during NREM sleep. Ripples in both regions were detected by thresholding the normalized squared LFP signal filtered between 100 Hz and 250 Hz. **b**, Colormap showing *Z*-scored signal surrounding the peak of each detected dorsal (left) and ventral ripple (right). **c**, Ripple rate calculated during NREM sleep in the dorsal (green) and ventral (purple) hippocampus (two-sided Mann–Whitney test, $^{****}P = 0.0007$; number of sessions, $N_{dHPC} = 40$, $N_{vHPC} = 47$). **d**, Coordinated events were defined as a pair of dorsoventral ripples that occurred within 100 ms of each other. Top: example dHPC and vHPC LFP traces showing one coordinated ripple. Bottom: percentage of coordinated events in the dHPC (green) and vHPC (purple) was different from chance level (dark green/purple) (two-sided Mann–Whitney test, $^{****}P_{dHPC} = 3.57 \times 10^{-8}$, $^{****}P_{vHPC} = 3.50 \times 10^{-8}$, $N_{Sessions} = 40$; whiskers extend to minimal and maximal data points; box edges are 25th and 75th percentiles; line represents median). **e**, Average autocorrelogram of ripple peaks for coordinated (green/purple) and uncoordinated (gray) ripples in the dHPC (top) and vHPC (bottom). **f**, Burst index of coordinated and uncoordinated ripples from the dHPC (left) and vHPC (right) (two-sided Mann–Whitney test, $^{****}P_{dHPC} = 8.85 \times 10^{-8}$, $^{*}P_{vHPC} = 0.002$, $N_{Sessions} = 40$). **g**, Response of dorsal (top) and ventral (bottom) HPC neurons to coordinated (green/purple) and uncoordinated (gray) ripples from the opposite side (paired Wilcoxon test, $^{****}P_{dHPC} = 4.9 \times 10^{-96}$, $^{*****}P_{vHPC} = 1.74 \times 10^{-15}$; number of single units, $N_{dHPC} = 856$, $N_{vHPC} = 461$; solid lines, mean; shaded areas, ±s.e.m.). **h**, Left: examples of significant dorsal replay events during dorsal ripples occurring within coordinated (top) and uncoordinated (bottom) ripple events. Right: ratio of the pre/post percentage of significant replay events for coordinated (red or blue) and uncoordinated (gray) dorsal ripples for aversive (red) and reward (blue) sessions (two-sided paired Wilcoxon test, $^{*}P_{aversive} = 0.02$, $P_{reward} = 0.77$; $N_{Sessions} = 40$; two-sided one-sample Wilcoxon test against one, $^{\#}P = 0.018$; black lines, mean; gray lines link paired observations). Max., maximum; min., minimum.

https://doi.org/10.1038/s41593-026-02252-w

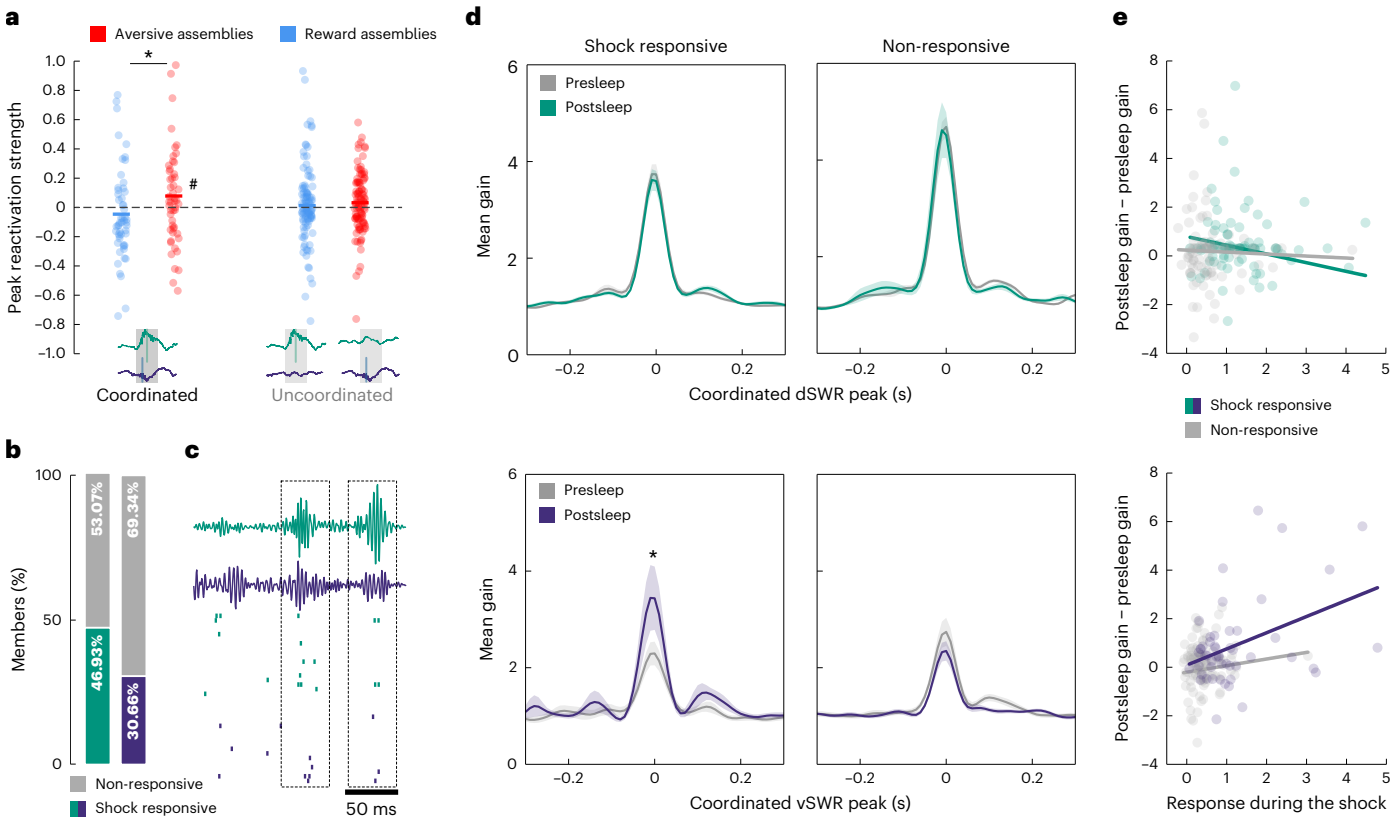

Fig. 7 | Shock-responsive ventral members increase their gain during dorsoventral coordinated ripples. a, Average peak reactivation strength for joint aversive and reward assemblies during dorsoventral coordinated ripples and dorsal or ventral uncoordinated ripples (non-paired two-way ANOVA, $P_{interaction} = 0.11$, $F = 2.45$, $^{*}P_{assembly\_type} = 0.02$, $F = 5.07$, $P_{ripple\_type} = 0.92$, $F = 0.01$. Tukey–Kramer post hoc test with Bonferroni correction, $^{*}P_{coordinated} = 0.024$, $P_{uncoordinated} = 0.25$). Only joint aversive assemblies showed a significant increase against zero (one-sided *t*-test, $^{\#}P = 0.04$; number of assemblies, $N_{Aversive} = 54$, $N_{Reward} = 53$). **b**, Percentage of shock-responsive neurons among dHPC (green) and vHPC (purple) members of joint aversive assemblies (dHPC, 46.93%; vHPC, 30.66%; χ^2: $P_{dHPC} = 0.71$, $P_{vHPC} = 0.40$). **c**, Example of two coordinated dorsoventral ripple events and associated single-unit activity (dashed boxes). **d**, Average gain in firing rate around coordinated ripple onset during NREM sleep preceding (gray) and following (green/purple) aversive runs (one-sided Mann–Whitney test, dHPC: $P_{Responsive} = 0.86$, $P_{Non\text{-}responsive} = 0.99$; number of units, $N_{Responsive} = 84$, $N_{Non\text{-}responsive} = 95$; vHPC: $^{*}P_{Responsive} = 0.039$, $P_{Non\text{-}responsive} = 0.99$, number of single units, $N_{Responsive} = 53$, $N_{Non\text{-}responsive} = 120$; solid lines, mean; shaded areas, ±s.e.m.). **e**, Linear correlation between the maximal response during the shock delivery and the change in gain between presleep and postsleep for coordinated ripple events (linear regression, dHPC: shock responsive, $R^2 = 0.01$, $P_{slope} = 0.32$; non-responsive, $R^2 = 0.001$, $P_{slope} = 0.77$; vHPC: shock responsive, $R^2 = 0.16$, $P_{slope} = 0.003$; non-responsive, $R^2 = 0.006$, $P_{slope} = 0.40$).

occur—we repeated the analysis using assemblies detected during quiet periods only and recalculated peak reactivation strength during coordinated and uncoordinated NREM ripples. Peak reactivation strength was not different from zero for either aversive or reward 'quiet' joint assemblies (Supplementary Fig. 11c). These results indicate that dorsoventral coordinated ripples constitute a permissive time window for the reinstatement of the representation of an aversive environment by the joint neural activity of the dHPC and vHPC.

We sought to identify the origin of the specific increase in peak reactivation strength for joint aversive assemblies. In particular, we hypothesized that vHPC shock-responsive neurons are key in this phenomenon. However, neither dorsal or ventral members of the joint aversive assemblies were enriched in shock-responsive units compared to the whole population of units from each region (Fig. 7b; vHPC, $\chi^2 = 0.71$, $P = 0.40$; dHPC: $\chi^2 = 0.13$, $P = 0.72$). Hippocampal neurons are globally massively recruited during SWRs, but experience modulates this recruitment[47]. We assessed the gain (that is, the normalized increase in activity) of each vHPC or dHPC member of the joint assemblies during coordinated SWRs before versus after the aversive or reward experience. Additionally, we distinguished between shock-responsive members and non-shock-responsive members (Fig. 7b,c). In the dHPC, neither the shock-responsive nor the non-responsive members showed an increase in gain during post-NREM coordinated SWRs compared to pre-NREM SWRs (Fig. 7d, top). However, in the vHPC, we found that shock-responsive members, but not non-responsive ones, significantly increased their activity during post-NREM coordinated SWRs (Fig. 7d, bottom). This response was specific to coordinated SWRs (Supplementary Fig. 12) and shock-responsive neurons, as there were no significant changes for reward-responsive neurons during coordinated or uncoordinated SWRs (Extended Data Fig. 10). Shock- and reward-responsive members of pure dHPC or vHPC assemblies also did not increase gain in coordinated or uncoordinated SWRs (Supplementary Fig. 13). Finally, we found a positive linear correlation between the change in activity gain during SWRs from presleep to postsleep and the level of activation during the shock experience selectively for ventral shock-responsive neurons (Fig. 7e). Altogether, these results suggest that the enhanced fidelity of joint reactivation after aversive experience is due to a selective increase in the participation of shock-responsive vHPC neurons to the coordinated assemblies during SWRs, originating in the intensity of their recruitment during the awake experience.

Discussion

In this study we detected dorsal, ventral and dorsoventral hippocampal neural assemblies during a similar spatial experience under two opposite valence conditions. We then tracked them during the subsequent

epochs to investigate the sleep-dependent reactivation mechanisms known to underlie memory consolidation within the dHPC and across the dHPC and other structures[15,16,48]. Our findings establish the existence of dorsoventral hippocampal coordinated reactivation during NREM sleep and provide further support for the independent reactivation of the vHPC[34]. In our task, the spatial context was stable and only the emotional valence changed. Given the respective roles of the dHPC and vHPC in spatial and emotional processing[4,23,24], and the corresponding dynamics of their neuronal assemblies (spatially tuned and preconfigured in the dHPC[7,46], versus emerging during emotional experience in the vHPC[12,38,49]), we expected dorsal assemblies to remain more consistent across the two conditions than ventral ones. Surprisingly, joint assemblies, rather than pure dorsal or ventral assemblies, better disambiguated the two conditions. The higher remapping of place cells between conditions in the vHPC compared to the dHPC contributed to the disambiguation. We hypothesize that dorsoventral coordination during acquisition and sleep-dependent processing allows functional binding of the stable spatial representation of the dHPC with the bimodal emotional aspect of the experience processed in the vHPC to compose an integrated, refined representation embedding all contextual parameters.

Both reward and aversive assemblies show reactivation during NREM sleep, which rapidly decay across the first 40 minutes of NREM sleep. Similar decays were previously reported for dorsal, ventral or dHPC–BLA reactivation[5,12,15]. Although quantitatively similar, the reactivations of the joint assemblies generated during the aversive versus reward conditions are qualitatively different: the reactivations of the aversive joint assemblies reflect more accurately the preceding experience compared to the reactivations of the reward assemblies. This effect depends on the strength of recruitment of the aversive assemblies during wakefulness and originates in the increased recruitment of vHPC shock-responsive neurons into the coordinated dorsal and ventral SWRs that support the joint reactivation. Coordinated SWRs following the aversive condition are also enriched in dorsal place-cell sequence replay. As such, they represent a privileged time window for binding spatial dHPC and emotional vHPC offline representations with heightened accuracy. As in most previous studies tackling sleep-dependent processing of emotional experience in the dHPC and other emotion-related structures[5,15], we did not find any reactivation during REM sleep, despite evidence of its role in emotional processing[50,51]. It is possible that the methods used to assess reactivation are not appropriate to the intrinsic dynamics of REM sleep or that the short epochs of REM sleep drastically reduce statistical power. Alternatively, REM sleep might contribute to emotional processing through mechanisms other than reactivation, such as synapse pruning and firing-rate homeostasis[52,53].

The salience of positive and negative stimuli cannot be perfectly matched, and the experimental design of the task to reach similar alternation behaviors in the two conditions constrained us to use rewards at fixed locations and shocks at varying locations. We also recorded at plateau performance to maximize data collection. Thus, it is possible that the lack of increase in peak reactivation strength for the reward condition is due to the high familiarity of the animal with the task and maze and that it would emerge following the exploration of a new environment. The increased accuracy we observed in the reactivation of the aversive assemblies may also be due to a higher salience of the shocks or to their less predictable nature. The vHPC was shown to be involved in both positive and negative emotional processing[35,36], but its role in processing the negative end of the valence spectrum has been more firmly established[22,23,26,27]. It is therefore also possible that the increased accuracy reflects an inherent 'fidelity' bias of the hippocampus toward negative information, reflected in the correlation between reactivation accuracy and recruitment strength during wakefulness only for the aversive assemblies.

SWRs also occur in wakefulness during non-locomotor behaviors, such as pausing for reward consumption. In that case, dorsal and ventral SWRs differentially activate neurons in a common structure target, the nucleus accumbens[35], suggesting that independent dorsal and ventral SWRs can separately route spatial and positive emotional information to common efferent structures. During sleep without prior learning, a small proportion of SWRs are coordinated between the dorsal and ventral poles[33,35]. We find that after an emotional spatial experience, this marginal subset of coordinated SWRs supports the reactivation of dorsoventral neuronal assemblies. Because during coordinated SWRs, the dSWR tends to precede the vSWR, we suggest that the extensive network of CA3 pyramidal cell collaterals and overlapping excitatory–inhibitory networks in CA1 or the direct projections from dCA2 to vCA1 (ref. 54) might allow for a subset of dSWRs to trigger vSWRs. A common input from the entorhinal cortex, subiculum or thalamic nuclei might also synchronize dorsal and ventral SWRs[2,3].

The vHPC shows intricate bidirectional connectivity patterns with the emotional network[3] that intersect with the functional diversity of vHPC cells[24,36], as exemplified by the preferential connectivity of vHPC shock-responsive cells with the basal amygdala[26]. The synchronization of dHPC and vHPC SWRs, associated with heightened spatioemotional precision, may account for previous reports of coordinated activity and replay between the dHPC and other regions, notably the basolateral amygdala and prefrontal cortex, despite the absence of direct anatomical connectivity[12,15,16,48]. Consistent with the literature[33,55], coordinated dvSWRs show a higher amplitude than isolated dSWRs or vSWRs, suggesting that they differentially affect activity brainwide and in direct output structures[56,57]. In the dHPC, SWRs display diverse features beyond amplitude, shaped by their inputs and constraining their neural content and outputs[58]. Similar diversity in the vHPC, combined with dorsoventral coordination, could enable highly precise control over information processing and transfer. Likewise, other heterogeneous NREM sleep patterns, such as dentate spikes[59], and their yet-unknown coordination across the dorsoventral hippocampal axis, may play complementary roles in consolidating complex memories. Overall, dHPC–vHPC coordination through SWRs emerges as a potential mechanism for integrating and broadcasting spatial and emotional representations, consistent with the established role of SWRs in memory consolidation and their widespread effects on the rest of the brain[8].

Online content

Any methods, additional references, Nature Portfolio reporting summaries, source data, extended data, supplementary information, acknowledgements, peer review information; details of author contributions and competing interests; and statements of data and code availability are available at https://doi.org/10.1038/s41593-026-02252-w.

References

1. Scoville, W. B. & Milner, B. Loss of recent memory after bilateral hippocampal lesions. *J. Neurol. Neurosurg. Psychiatry* **20**, 11–21 (1957).
2. Strange, B. A., Witter, M. P., Lein, E. S. & Moser, E. I. Functional organization of the hippocampal longitudinal axis. *Nat. Rev. Neurosci.* **15**, 655–669 (2014).
3. Pronier, É, Morici, J. F. & Girardeau, G. The role of the hippocampus in the consolidation of emotional memories during sleep. *Trends Neurosci.* **46**, 912–925 (2023).
4. O'Keefe, J. Place units in the hippocampus of the freely moving rat. *Exp. Neurol.* **51**, 78–109 (1976).
5. Wilson, M. A. & McNaughton, B. L. Reactivation of hippocampal ensemble memories during sleep. *Science* **265**, 676–679 (1994).
6. Girardeau, G. & Lopes-dos-Santos, V. Brain neural patterns and the memory function of sleep. *Science* **374**, 560–564 (2021).
7. van de Ven, G. M. et al. Hippocampal offline reactivation consolidates recently formed cell assembly patterns during sharp wave-ripples. *Neuron* https://doi.org/10.1016/j.neuron.2016.10.020 (2016).

8. Buzsáki, G. Hippocampal sharp wave-ripple: a cognitive biomarker for episodic memory and planning. *Hippocampus* **25**, 1073–1188 (2015).
9. Girardeau, G., Benchenane, K., Wiener, S. I., Buzsáki, G. & Zugaro, M. B. Selective suppression of hippocampal ripples impairs spatial memory. *Nat. Neurosci.* **12**, 1222–1223 (2009).
10. Wang, D. V. et al. Mesopontine median raphe regulates hippocampal ripple oscillation and memory consolidation. *Nat. Neurosci.* **18**, 728–735 (2015).
11. Gridchyn, I., Schoenenberger, P., O'Neill, J. & Csicsvari, J. Assembly-specific disruption of hippocampal replay leads to selective memory deficit. *Neuron* **106**, 291–300 (2020).
12. Miyawaki, H. & Mizuseki, K. De novo inter-regional coactivations of preconfigured local ensembles support memory. *Nat. Commun.* **13**, 1272 (2022).
13. Todorova, R. & Zugaro, M. Hippocampal ripples as a mode of communication with cortical and subcortical areas. *Hippocampus* **30**, 39–49 (2020).
14. Buzsáki, G. Neural syntax: cell assemblies, synapsembles, and readers. *Neuron* **68**, 362–385 (2010).
15. Girardeau, G., Inema, I. & Buzsáki, G. Reactivations of emotional memory in the hippocampus-amygdala system during sleep. *Nat. Neurosci.* **20**, 1634–1642 (2017).
16. Lansink, C. S., Goltstein, P. M., Lankelma, J. V., Mcnaughton, B. L. & Pennartz, C. M. A. Hippocampus leads ventral striatum in replay of place-reward information. *PLoS Biol.* **7**, e1000173 (2009).
17. Moita, M. A. P., Rosis, S., Zhou, Y., LeDoux, J. E. & Blair, H. T. Putting fear in its place: remapping of hippocampal place cells during fear conditioning. *J. Neurosci.* **24**, 7015–7023 (2004).
18. Blair, G. J. et al. Hippocampal place cell remapping occurs with memory storage of aversive experiences. *eLife* **12**, e80661 (2023).
19. Kim, E. J. et al. Alterations of hippocampal place cells in foraging rats facing a predatory threat. *Curr. Biol.* **25**, 1362–1367 (2015).
20. Malik, R., Li, Y., Schamiloglu, S. & Sohal, V. S. Top-down control of hippocampal signal-to-noise by prefrontal long-range inhibition. *Cell* **185**, 1602–1617 (2022).
21. Harvey, R. E., Robinson, H. L., Liu, C., Oliva, A. & Fernandez-Ruiz, A. Hippocampo-cortical circuits for selective memory encoding, routing, and replay. *Neuron* **111**, 2076–2090 (2023).
22. Forro, T. et al. Anxiety-related activity of ventral hippocampal interneurons. *Prog. Neurobiol.* **219**, 102368 (2022).
23. Jimenez, J. C. et al. Anxiety cells in a hippocampal-hypothalamic circuit. *Neuron* **97**, 670–683 (2018).
24. Ciocchi, S., Passecker, J., Malagon-Vina, H., Mikus, N. & Klausberger, T. Selective information routing by ventral hippocampal CA1 projection neurons. *Science* **348**, 560–563 (2015).
25. Li, K., Koukoutselos, K., Sakaguchi, M. & Ciocchi, S. Distinct ventral hippocampal inhibitory microcircuits regulating anxiety and fear behaviors. *Nat. Commun.* **15**, 8228 (2024).
26. Jimenez, J. C. et al. Contextual fear memory retrieval by correlated ensembles of ventral CA1 neurons. *Nat. Commun.* **11**, 3492 (2020).
27. Herbst, M. R., Twining, R. C. & Gilmartin, M. R. Ventral hippocampal shock encoding modulates the expression of trace cued fear. *Neurobiol. Learn. Mem.* **190**, 107610 (2022).
28. Pitkänen, A., Pikkarainen, M., Nurminen, N. & Ylinen, A. reciprocal connections between the amygdala and the hippocampal formation, perirhinal cortex, and postrhinal cortex in rat: a review. *Ann. N. Y. Acad. Sci.* **911**, 369–391 (2000).
29. Huff, M. L., Emmons, E. B., Narayanan, N. S. & LaLumiere, R. T. Basolateral amygdala projections to ventral hippocampus modulate the consolidation of footshock, but not contextual, learning in rats. *Learn. Mem.* **23**, 51–60 (2016).
30. Wang, G.-W., Liu, J. & Wang, X.-Q. Post-training reversible disconnection of the ventral hippocampal–basolateral amygdaloid circuits impairs consolidation of inhibitory avoidance memory in rats. *Learn. Mem.* **24**, 602–606 (2017).
31. Shiozaki, H., Kuga, N., Kayama, T., Ikegaya, Y. & Sasaki, T. Selective serotonin reuptake inhibitors suppress sharp wave ripples in the ventral hippocampus. *J. Pharmacol. Sci.* **152**, 136–143 (2023).
32. Kuga, N. et al. Hippocampal sharp wave ripples underlie stress susceptibility in male mice. *Nat. Commun.* **14**, 2105 (2023).
33. Patel, J. et al. Local generation and propagation of ripples along the septotemporal axis of the hippocampus. *J. Neurosci.* **33**, 17029–17041 (2013).
34. Nguyen, R., Koukoutselos, K., Forro, T. & Ciocchi, S. Fear extinction relies on ventral hippocampal safety codes shaped by the amygdala. *Sci. Adv.* **9**, eadg4881 (2023).
35. Sosa, M., Joo, H. R. & Frank, L. M. Dorsal and ventral hippocampal sharp-wave ripples activate distinct nucleus accumbens networks. *Neuron* **105**, 725–741 (2020).
36. Shpokayte, M. et al. Hippocampal cells segregate positive and negative engrams. *Commun. Biol.* **5**, 1–15 (2022).
37. Kim, J., Pignatelli, M., Xu, S., Itohara, S. & Tonegawa, S. Antagonistic negative and positive neurons of the basolateral amygdala. *Nat. Neurosci.* **19**, 1636–1646 (2016).
38. Biane, J. S. et al. Neural dynamics underlying associative learning in the dorsal and ventral hippocampus. *Nat. Neurosci.* **26**, 798–809 (2023).
39. Barth, A. M., Jelitai, M., Vasarhelyi-Nagy, M. F. & Varga, V. Aversive stimulus-tuned responses in the CA1 of the dorsal hippocampus. *Nat. Commun.* **14**, 6841 (2023).
40. Góis, Z. H. T. D. & Tort, A. B. L. Characterizing speed cells in the rat hippocampus. *Cell Rep.* **25**, 1872–1884 (2018).
41. Hebb, D. O. *The Organization of Behavior: A Neuropsychological Theory* (Wiley, 1949).
42. Oberto, V. J. et al. Distributed cell assemblies spanning prefrontal cortex and striatum. *Curr. Biol. CB* **32**, 1–13 (2022).
43. Lopes-dos-Santos, V., Ribeiro, S. & Tort, A. B. L. Detecting cell assemblies in large neuronal populations. *J. Neurosci. Methods* **220**, 149–166 (2013).
44. Gomperts, S. N., Kloosterman, F. & Wilson, M. A. VTA neurons coordinate with the hippocampal reactivation of spatial experience. *eLife* **4**, 321–352 (2015).
45. Diba, K. & Buzsáki, G. Forward and reverse hippocampal place-cell sequences during ripples. *Nat. Neurosci.* **10**, 1241–1242 (2007).
46. Farooq, U., Sibille, J., Liu, K. & Dragoi, G. Strengthened temporal coordination within pre-existing sequential cell assemblies supports trajectory replay. *Neuron* **103**, 719–733 (2019).
47. Ormond, J., Serka, S. A. & Johansen, J. P. Enhanced reactivation of remapping place cells during aversive learning. *J. Neurosci.* https://doi.org/10.1523/JNEUROSCI.1450-22.2022 (2023).
48. Lansink, C. S. et al. Preferential reactivation of motivationally relevant information in the ventral striatum. *J. Neurosci.* **28**, 6372–6382 (2008).
49. Pompili, M. N., Hamou, N. & Wiener, S. I. Integration of fear learning and fear expression across the dorsoventral axis of the hippocampus. *Proc. Natl Acad. Sci. USA* https://doi.org/10.1073/pnas.2520207123 (2026).
50. Boyce, R., Glasgow, S. D., Williams, S. & Adamantidis, A. Causal evidence for the role of REM sleep theta rhythm in contextual memory consolidation. *Science* **352**, 812–816 (2016).
51. Tempesta, D., Socci, V., De Gennaro, L. & Ferrara, M. Sleep and emotional processing. *Sleep. Med. Rev.* **40**, 183–195 (2018).

52. Grosmark, A. D., Mizuseki, K., Pastalkova, E., Diba, K. & Buzsáki, G. REM sleep reorganizes hippocampal excitability. *Neuron* **75**, 1001–1007 (2012).
53. Li, W., Ma, L., Yang, G. & Gan, W. B. REM sleep selectively prunes and maintains new synapses in development and learning. *Nat. Neurosci.* **20**, 427–437 (2017).
54. Meira, T. et al. A hippocampal circuit linking dorsal CA2 to ventral CA1 critical for social memory dynamics. *Nat. Commun.* **9**, 4163 (2018).
55. De Filippo, R. & Schmitz, D. Differential ripple propagation along the hippocampal longitudinal axis. *eLife* **12**, e85488 (2023).
56. Nitzan, N., Swanson, R., Schmitz, D. & Buzsáki, G. Brain-wide interactions during hippocampal sharp wave ripples. *Proc. Natl Acad. Sci. USA* **119**, e2200931119 (2022).
57. Ramirez-Villegas, J. F., Logothetis, N. K. & Besserve, M. Diversity of sharp-wave–ripple LFP signatures reveals differentiated brain-wide dynamical events. *Proc. Natl Acad. Sci. USA* **112**, 11084–11089 (2015).
58. Castelli, M., Lopes-Dos-Santos, V., Gava, G. P., Lambiotte, R. & Dupret, D. Hippocampal ripple diversity organizes neuronal reactivation dynamics in the offline brain. *Neuron* **113**, 4245–4262 (2025).
59. Farrell, J. S., Hwaun, E., Dudok, B. & Soltesz, I. Neural and behavioural state switching during hippocampal dentate spikes. *Nature* **628**, 590–595 (2024).

Methods

Ethical statement

All experimental procedures were performed following the official European guidelines for the care and use of laboratory animals (86/609/EEC) and the Policies of the French Committee of Ethics (decree nos. 87-848 and 2001–464), and after approval by ethical committee (APAFIS #35991-2022031810445522 v3).

Subjects and electrode implantation

This project included six individually housed female Long–Evans rats (Charles Rivers Laboratories) maintained on a 12 h:12 h light–dark cycle. Animals (300 g/3 months old at the time of the surgery) were injected with buprenorphine (Vetergesic, 0.3 mg ml^{-1}, dose 0.05 mg kg^{-1}) and deeply anesthetized with isoflurane. The local anesthetic Lidocaine (Lidor, 20 mg ml^{-1}, dose 4 mg kg^{-1}) was subcutaneously injected into the scalp 15 min before skin incision. The body temperature was monitored throughout the surgery and maintained at 37 °C using a heating pad. Small metal screws were placed at different points in the skull to anchor the implant, and two screws were implanted above the cerebellum to serve as ground and reference. Two or three electrodes (NeuroNexus Buzsaki64L for the vHPC, Buzsaki 32 or tetrode array for the dHPC) mounted on individual movable nano-drives (Cambridge nano-drives, size 2 mm × 5 mm × 11 mm) were implanted above the vHPC unilaterally (initial position: anteroposterior, −5.50 mm; lateral, 4.10 mm; dorsoventral, −6.5 mm; angle, 10°) and in the dHPC either unilaterally or bilaterally (initial position: anteroposterior, −3.50 mm; lateral, 2.50 mm; dorsoventral, −1.7 mm). The drives were secured on the skull using dental cement. The drives and probes were protected by a cement-covered copper mesh Faraday cage on which the probe connectors were attached. For the eyelid stimulation, a bipolar electrode made of two 140-µm silver wires was inserted between the skin and the muscle surrounding the eyelid. The connectors were fixed to the copper mesh. Following the surgery, animals were injected with a combination of buprenorphine (Vetergesic, 0.3 mg ml^{-1}, dose 0.05 mg kg^{-1}) and meloxicam (Metacam, 5 mg ml^{-1}, dose 1 mg ml^{-1}) at 24 h and 48 h. Animals were allowed to recover for at least 5 days with ad libitum food and water before training started. In one animal, the dHPC electrode failed to reach the pyramidal layer and only vHPC data was used.

Recordings and behavior

All animals were free from prior manipulation before being included in the study. All experiments were performed during the light cycle. After at least 5 days of daily handling, animals were water-deprived and trained to run back and forth on a linear track for water rewards. After 7 days of training, animals regained access to ad libitum water, and they underwent electrode implantation surgery 3 days later. After the recovery period, animals were water-deprived again and re-exposed to the reward linear track task for at least 2 days. Subsequently, animals were exposed to three daily training sessions composed of a reward and an aversive linear track exploration. For pretraining on the aversive run condition, animals were initially provided with water at the end of each lap for a certain time; the remainder of the time, they received an electric shock to the eyelid if they remained motionless for at least 20 s. The reward time was progressively reduced across training days until shocks were delivered only if the animal remained quiet. Once the animals were pretrained, task sessions were composed of pure reward and pure aversive run sessions, preceded and followed by sleep sessions (Fig. 1a,b). Across days, the aversive and reward runs were presented in a pseudorandomized order, ensuring that both the aversive–reward and reward–aversive combinations occurred approximately the same number of times over the course of the experiment. At the end of each recording day, animals had access to ad libitum water for 5–20 min to ensure the animals remained at >80% of their normal weight. During pretraining, the probes were slowly lowered in the brain to reach the dorsal and ventral CA1 pyramidal layers. Afterward, the probes were adjusted daily to optimize ripple and unit recording. Signals were recorded at 20 kHz using an Intan recording system (Intan Technologies), and videos were captured at 30 fps with a Basler camera (ace Basler 106754) synchronized with the Intan system. The instantaneous speed was calculated using the neck position extracted from the videos using DeepLab Cut (DeepLabCut2.0 Toolbox)[60].

Preprocessing

Electrophysiological data were sampled at 20 kHz and downsampled to 1,250 Hz to extract the LFPs. Spikes were extracted by high-pass filtering and thresholding the signal and then clustered using Kilosort 2.5 followed by manual curation using Phy. Sleep stages were manually scored through visual inspection of the dorsal and ventral hippocampal spectrograms and accelerometer signals using TheStateEditor, a custom program from the FMA toolbox (http://fmatoolbox.sourceforge.net/). We defined NREM epochs as periods characterized by immobility and low theta/delta ratio, whereas REM sleep was characterized by immobility and regular theta waves (Supplementary Fig. 5a–c). Ripple detection was performed by band-pass filtering (~100–200 Hz), squaring, *Z*-scoring and thresholding the LFP recorded in the dorsal or ventral CA1 pyramidal layer. Ripples were defined as events lasting between 20 ms and 100 ms, starting at 2 or 3 s.d. above the mean and peak amplitude exceeding 5 or 7 s.d. for dorsal or ventral ripples, respectively.

Statistics and reproducibility

All analyses were performed using customized toolboxes (Chronux, FMA toolbox), built-in functions and custom-written scripts in Matlab (The MathWorks, Inc.). If the data met the criteria for normality, we used Student's *t*-tests for two-group comparisons and one-way analysis of variance (ANOVA) followed by the Tukey–Kramer post hoc test for multiple-group comparisons. A two-way ANOVA was used to assess the effects of two independent variables, each with multiple levels, followed by Bonferroni-adjusted Tukey–Kramer post hoc tests for pairwise comparisons between groups. If data did not meet normality criteria, we used a two-tailed unpaired Mann–Whitney test for comparisons between two groups. For more than two groups, we used the Kruskal–Wallis test for unpaired data and the Friedman test for paired data, followed by the Tukey–Kramer post hoc test for pairwise comparisons between groups. Data presented in cumulative graphs were compared using the Kolmogórov–Smirnov test. Correlations between continuous variables were examined by linear regression. A value of $P < 0.05$ was considered statistically significant unless otherwise stated. Data were presented as boxplots, where the edges of the box represent the 25th and 75th percentiles and the central line indicates the median, or as scatterplots showing individual data points together with the mean. No statistical method was used to predetermine sample size, which was chosen according to the standards in the field. Sessions including fewer than three neurons in the dHPC or vHPC were excluded for the detection of assemblies and PCA ('Single-unit analyses' and 'Assembly analysis' sections). We excluded the data from the dorsal hippocampal electrode of rat 126 because the electrode did not reach the pyramidal layer. The order of the aversive and reward sessions was pseudorandomized. Due to the nature of the experimental design, the investigators could not be blinded to allocation during experiments and outcome assessment.

Dorsoventral ripple coordination

First, we constructed a cross-correlogram of vSWR peaks locked to dorsal ones using the CCG function from FMAtoolbox and normalized it to the total number of vSWRs (10-ms bins). By visually inspecting the cross-correlogram, we defined coordinated events as dorsoventral ripple pairs occurring ±100 ms from each other. To ascertain whether the percentage of coordinated dorsal and ventral ripples exceeded the chance level, we shuffled the reference ripple peaks 100 times and calculated the percentage of coordinated reference ripples.

This process yielded a surrogate average percentage value compared with the value obtained in each session. For autocorrelograms and cross-correlograms in Fig. 6, we used 10-ms bins. Directionality inside each dorsoventral coordinated ripple pair was calculated as the percentage of coordinated ripple events in which the dorsal ripple preceded the ventral one and vice versa (Extended Data Fig. 9).

Single-unit analyses

We detected 1,071 single units in the dHPC and 544 in the vHPC in six animals. Units were classified into putative pyramidal cells and putative interneurons based on waveform shape (Extended Data Fig. 3): duration at 50% from baseline to peak (distance A) and peak-to-trough time (distance B) were used for clustering with *k*-means into two clusters, interneurons and pyramidal cells. The gain locked to ripple peaks was calculated in a 10-ms bin by dividing the firing rate in each bin by the baseline firing rate outside SWRs (inter-ripple NREM intervals). To define whether a unit was ripple-modulated, we performed a Poisson test with $P < 0.001$ (Supplementary Fig. 5d,e). For Fig. 2c, PCA was performed on the spike trains of all dorsal and ventral hippocampal neurons separately. Because the number of PCA dimensions is related to the number of neurons recorded, we included only sessions with at least three single units. We concatenated periods when the animal was exploring the environment (>7 cm s^{-1} for more than 2 s) during aversive and reward run sessions. We then measured the Euclidean distance between the centroids of the aversive and reward projections[61].

Place cells were defined in the dHPC and vHPC as putative pyramidal cells with spatial information content[62] exceeding the 90th quantile of the chance distribution and the presence of at least one place field in at least one of the two run conditions. Chance distribution was assessed by circularly permuting position data relative to spike times for each unit. To construct the place tuning curve, position data were discretized into 2.5-cm bins, and rate maps were computed as smoothed firing-rate histograms (Gaussian kernel, sigma = 2) normalized by occupancy time per bin. Data from the ends of the linear track, where rewards were delivered, were excluded from the analysis. Only periods during which the animals maintained speed higher than 2.5 cm s^{-1} were considered. Place fields were defined as contiguous regions comprising a minimum of four spatial bins (10 cm) that contained the location of the maximum firing-rate peak (≥1 Hz). Within these regions, firing rates were required to exceed 60% of the peak firing-rate value.

To evaluate remapping, we calculated spatial correlations as bin-by-bin Pearson's correlations of the rate maps, both within and between conditions. For within-condition comparisons, position and spike data from a given condition were divided into *n* bins of 1 s each, and bins were randomly assigned into two groups of size *n*/2. Separate rate maps were generated for each group, and their spatial correlation was computed. This procedure was repeated 100 times per cell, and the mean correlation was reported. For between-condition comparisons, data from each condition were similarly divided into two groups to construct a rate map. To compute the spatial correlation, one of the two rate maps from each condition was randomly chosen. This process was repeated 100 times per cell, and the mean was reported[63].

To assess the unit response to shocks or rewards, the firing rate of each single unit was computed using 100-ms time bins in (±5 s) centered around the time of shock delivery or reward delivery and *Z*-scored. The reward was delivered upon the opening of the water valve triggered automatically by the passage of the rat through infrared detectors placed at the entrance of the track end platform (schematic Fig. 3h). The average delay from reward delivery to reaching reward location was 0.93 ± 0.02 s. To identify reward or shock-responsive units, a surrogate distribution was generated by averaging the responses following the shock/reward after shuffling the spike times 200 times. Units with a firing rate exceeding the 90th percentile of this surrogate distribution were classified as shock responsive or reward responsive.

To identify speed-modulated units, linear correlations between firing rates and mean speed outside of the shock periods were calculated in 1-s bins. Units with a *P* value < 0.05 were considered speed-modulated. To remove the linear influence of speed on neural responses during shock delivery or approaching the reward port, the Gram–Schmidt orthogonalization process was applied[64,65]. Briefly, the mean neuronal activity was projected onto the mean speed trace, and the residual component was used for subsequent analysis. For statistical comparisons and plotting (Fig. 3a,d–f,j) of the response during the shock or reward before and after speed decorrelation, the maximum response value during the shock was used after each trace was normalized to its baseline period (from −5 s to −1 s before the shock or reward).

Response during coordinated ripples

The firing rate of each pyramidal cell was calculated in 10-ms bins and smoothed using a 2-s.d. Gaussian kernel. Each tuning curve was then normalized by the mean firing rate during NREM sleep outside of ripple events. For coordinated and uncoordinated ripples, the perievent firing rate was calculated within ±500 ms of the ripple event. These firing-rate curves were further normalized by the mean firing rate of each tuning curve, calculated in a time window ±200 ms from the event. The firing activity from dorsal and ventral pyramidal cells was locked to the coordinated dorsal or ventral ripple member, respectively. Statistical comparisons of pre- and post-NREM ripple mean gains were performed using a one-sided Mann–Whitney test on the maximal gain in a ±300-ms window centered at the ripple peak. To correlate the shock-induced response with the response during sleep, the difference between the average response during coordinated ripples in post-NREM and pre-NREM sleep was linearly correlated with the maximal response during shock delivery in the aversive run.

Assembly analysis

Assembly detection was performed only in sessions having at least three neurons in the dHPC or vHPC that were active in both conditions. We binned and *Z*-scored the spike trains of dorsal and ventral pyramidal cells during mobility periods (>7 cm s^{-1} during more than 2 s) into 25-ms bins, considered the optimal bin for assembly detection[7]. Assembly patterns were identified using a two-step process using ICA and PCA[43] (Supplementary Fig. 2). After detecting the assembly patterns, units with weights exceeding the threshold defined as abs($1/\sqrt{N}$) were defined as assembly members. Assemblies with members in both the dHPC and vHPC were defined as joint assemblies.

Assembly pattern analyses

To track assembly pattern expression over time (Supplementary Fig. 2), a projection matrix was created for each pattern using its weight vector's outer product, with the main diagonal set to zero. To maximize the role of members in assembly activations, we set to zero the weight of non-member units. Each neuron's spike train was convolved with a Gaussian kernel and *Z*-scored. The expression strength of a pattern at any time was defined by the quadratic form of its projection matrix with the smoothed and *Z*-scored firing-rate vector. A peak was defined as strength > 5. We calculated the peak rate in 60-s windows during presleep and postsleep. To assess assembly activation dynamics in the real-time course of post-NREM sleep, peak rates were normalized to the average rate during pre-NREM sleep and aligned to the onset of the first post-NREM epoch. To minimize the overlap between the postsleep of the first emotional condition and the presleep of the second one, we restricted NREM or REM epochs to those occurring 1 h before or after each run session. Peak reactivation strength was calculated as the average values of peaks occurring during postsleep NREM minus the average of the peak values in presleep NREM divided by the average value of all peaks detected during both sleep sessions. The calculation was restricted to peaks occurring during NREM periods or ripples.

Replay detection

The replay sequence detection algorithm was implemented using the code provided by ref. 66. Candidate replay events were defined as dorsal ripples containing at least three active place cells. To evaluate whether these events carried spatial information, we first applied a Bayesian reconstruction method. Briefly, given the average firing rate $f_i(x)$ for n dorsal hippocampal neurons, we estimated the animal's location x given the number of spikes n of all the cell within a time window τ, where n is the number of dorsal hippocampal place cells and $P(x)$ is the probability of a certain position being reactivated:

$$P(x,|,n) = P(x)\left(\prod_{i=1}^{N} f_i(x)^{n_i}\right)\exp\left(-\tau\sum_{i=i}^{N} f_i(x)\right)$$

As a complementary approach, we used a previously described template-based rank-order correlation method[45,66]. This method correlates the order of place-field activation on the linear track with the spike sequence observed during a candidate replay event. Candidate replay events were discretized into 20-ms bins across the ripple duration, producing a posterior probability matrix (position × time). To identify sequential trajectories, the Radon transform[67] was applied to this matrix, and the integral of the best-fit line was calculated to quantify the strength of linear trajectories consistent with replay. For both methods, significance was determined by comparing observed values to surrogate distributions obtained by circularly shuffling place-cell IDs. A candidate was classified as significant if it exceeded the 90th percentile of its corresponding surrogate distribution. Because uncoordinated ripple events were more frequent than coordinated ones, they were subsampled 1,000 times, and the mean percentage of significant replays was computed.

Reporting summary

Further information on research design is available in the Nature Portfolio Reporting Summary linked to this article.

Data availability

The data that support the findings of this study will be made available upon reasonable request.

Code availability

All codes used to generate the figures are available on the Girardeau Lab GitHub repository (https://github.com/GirardeauLab/Morici_2026).

References

60. Mathis, A. et al. DeepLabCut: markerless pose estimation of user-defined body parts with deep learning. *Nat. Neurosci.* **21**, 1281–1289 (2018).
61. Elmore, K. L. & Richman, M. B. Euclidean distance as a similarity metric for principal component analysis. *Mon. Weather Rev.* **129**, 540–549 (2001).
62. Skaggs, W. E., McNaughton, B. L. & Gothard, K. M. An information-theoretic approach to deciphering the hippocampal code. *Adv. Neural Inf. Process. Syst.* **5**, 1030–1037 (1993).
63. Nagelhus, A., Andersson, S. O., Gonzalo Cogno, S., Moser, E. I. & Moser, M. B. Object-centered population coding in CA1 of the hippocampus. *Neuron* **111**, 2091–21044 (2023).
64. Eichele, T. et al. Assessing the spatiotemporal evolution of neuronal activation with single-trial event-related potentials and functional MRI. *Proc. Natl Acad. Sci. USA* **102**, 17798–17803 (2005).
65. Shahidi, N. et al. Population coding of strategic variables during foraging in freely moving macaques. *Nat. Neurosci.* **27**, 772–781 (2024).
66. Tingley, D. & Peyrache, A. On the methods for reactivation and replay analysis. *Philos. Trans. R. Soc. Lond. B Biol. Sci.* **375**, 20190231 (2020).
67. Davidson, T. J., Kloosterman, F. & Wilson, M. A. Hippocampal replay of extended experience. *Neuron* **63**, 497–507 (2009).

Acknowledgements

We thank R. Todorova, N. Karalis, K. Studeničová, O. Peron and all Girardeau lab members for insightful discussions and advice on analysis. We are grateful to L. Clément and M. Sarraudy for assistance with pilot experiments, to B. Khouader for his contribution to the experimental setup and to B. Lecomte, E. Marsan and all the zootechnician team for animal care. This work was funded by ATIP-Avenir, Fondation Schlumberger for Education and Research, grant nos. ANR-22-CE37-0020 and ANR-22-CE92-0019 (G.G.); Fondation Fyssen (G.G., J.F.M., A.S.); grant no. EMBO 275-2021 (J.F.M.) and Sorbonne Université (I.L.-P.). The funders had no role in study design, data collection and analysis, decision to publish or preparation of the manuscript.

Author contributions

J.F.M. and G.G. conceptualized the study. E.P., I.L.-P. and J.F.M. performed the experiments. A.S. and J.F.M. analyzed the data. J.F.M. and G.G. wrote the paper with contributions from all authors.

Competing interests

The authors declare no competing interests.

Additional information

Extended data is available for this paper at https://doi.org/10.1038/s41593-026-02252-w.

Supplementary information The online version contains supplementary material available at https://doi.org/10.1038/s41593-026-02252-w.

Correspondence and requests for materials should be addressed to Gabrielle Girardeau.

Peer review information *Nature Neuroscience* thanks Jeremy Biane, Antonio Fernandez-Ruiz, Mazen Kheirbek and the other, anonymous, reviewer(s) for their contribution to the peer review of this work.

https://doi.org/10.1038/s41593-026-02252-w

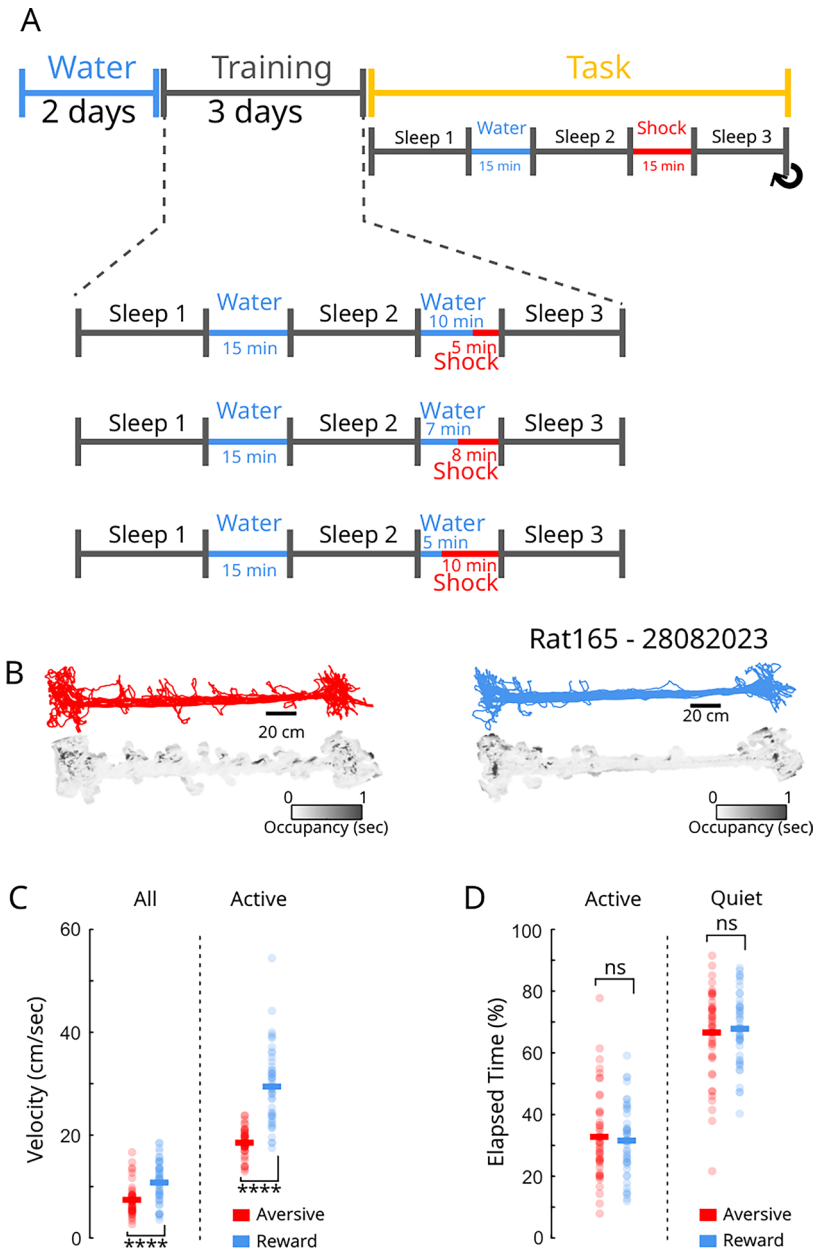

Extended Data Fig. 1 | Training protocol and behavioral characterization. **A**, After the implantation surgery, animals were re-trained to perform the rewarded run ('Water'). Then for 3 days, the shock was gradually introduced and water rewards eliminated to train the animals on the aversive run ('Training'). For the following days, animals performed the rewarded and aversive runs on the same day, starting with the rewarded or aversive run in alternation (Task). The recordings started when they reached plateau performance for both run types (see Main text and Fig.1). **B**, Examples trajectories and occupancy maps (grey) for aversive (red) and rewarded-motivated exploration (blue). Active periods were defined as moments where the animals showed an instantaneous speed of >7 cm/sec for at least 2 seconds. **C**, Average velocity for aversive and rewarded-run sessions during the whole run (left) or during the active period only (right) (Two-sided t test, ****$p = 8.51e^{-6}$; $N_{Sessions} = 47$; Solid lines: mean; shaded areas: ±SEM). **D**, Time spent in the active and quiet state on the track (Two-sided t test, $p = 0.62$, $N_{Sessions} = 47$; Solid lines: mean).

https://doi.org/10.1038/s41593-026-02252-w

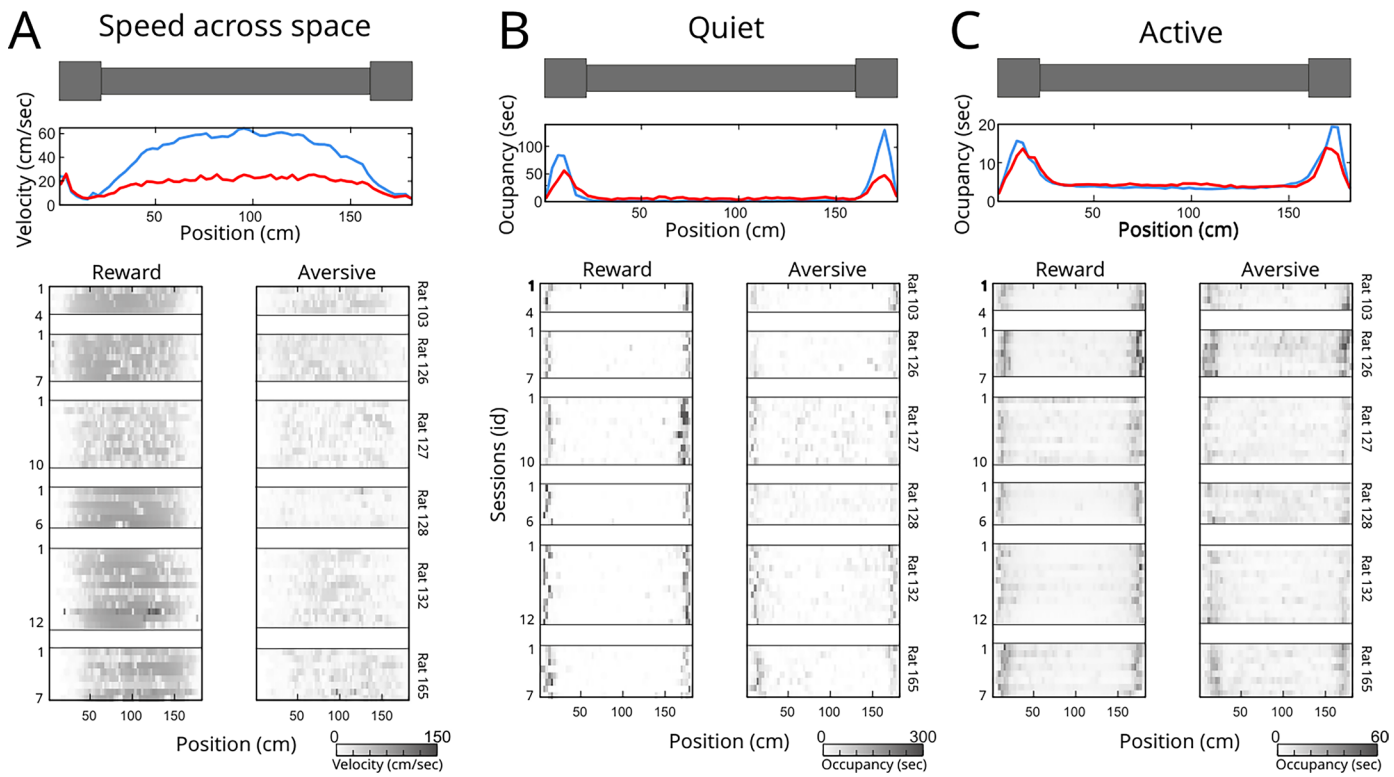

Extended Data Fig. 2 | Distribution of speed, quiet, and active periods across the linear track. A, Average speed as a function of location on the track for all aversive (red; N = 47) and rewarded runs (blue; n = 47; top) and for individual runs (greyscale; bottom). **B**, Average time spent in quiet behavior (<7 cm/sec) as a function of location on the track for all runs (top) and individual runs (bottom;greyscale). **C**, Same as **B** but for active behavior.

https://doi.org/10.1038/s41593-026-02252-w

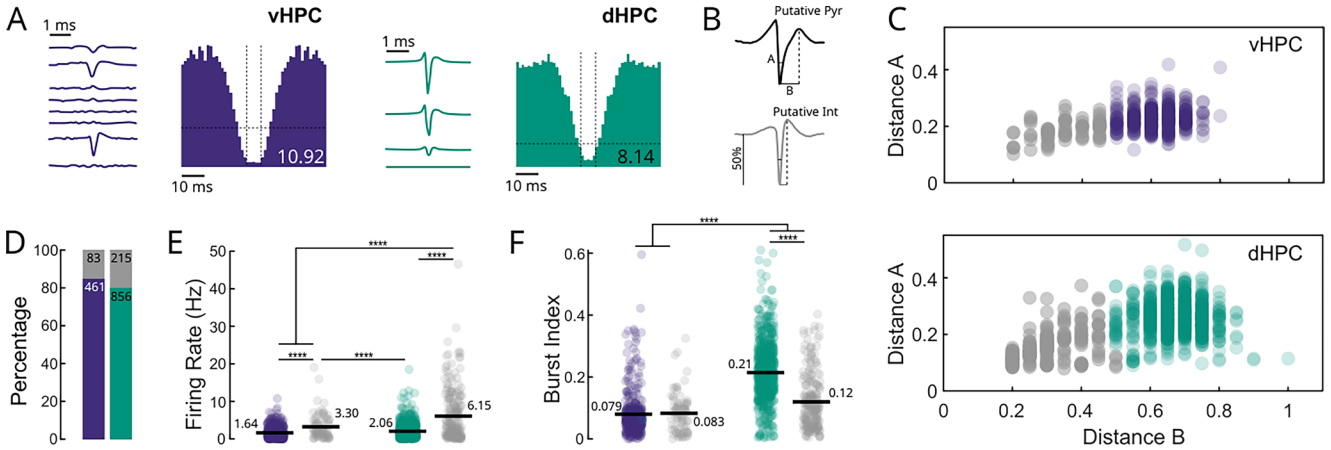

Extended Data Fig. 3 | Single-units waveform classification and characterization. A, Examples of ventral (left panel, purple) and dorsal (right panel, green) single units. **B**, Units were classified into putative pyramidal cells (Pyr) or putative interneurons (Int) using k-means clustering with 2 clusters on duration at 50% from baseline to peak (distance A) and peak-to-trough time (distance B). **C**, The clustering into putative pyramidal cells (green/purple) and putative interneurons (grey) was performed separately in the vHPC (top) and dHPC (bottom). **D**, Percentage of Pyr (green/purple) and Int. (grey) in the dHPC (green, Number of Single-Units: $N_{int} = 215$, $N_{pyr} = 856$) and vHPC (purple, Number of Single-Units, $N_{int} = 83$, $N_{pyr} = 461$). **E**, Firing rates of putative Pyr and Int. in the vHPC (purple) and dHPC (green) (Two-way ANOVA, $p_{cell\_type} = 2.31e^{-34}$, $F = 177.73$, $p_{structure} = 1.51e^{-13}$, $F = 57.73$, pinteraction=$1.68e^{-8}$, $F = 31.76$, Bonferroni post-hoc test, Pyr vs Int: pvHPC=0.0002, $p_{dHPC} = 3.77e^{-9}$, $p_{dHPC\text{-}vHPC} = 0.007$, $p_{vHPC\text{-}dHPC} = 3.76e^{-9}$, Int vs Int: $p_{dHPC\text{-}vHPC} = 3.78e^{-9}$, Pyr vs Pyr: $p_{dHPC\text{-}vHPC} = 0.15$; Number of Single-Units, dHPC: $N_{int} = 215$, $N_{pyr} = 856$, vHPC: $N_{int} = 83$, $N_{pyr} = 461$; Solid lines: mean). **F**, Burst index for Pyr. and Int. in the vHPC and dHPC (Two-way ANOVA, $p_{cell\_type} = 3.79e^{-12}$, $F = 49.07$, $p_{structure} = 9.24e^{-48}$, $F = 227.12$, $p_{interaction}9 = .16e^{-15}$, $F = 61.36$, Bonferroni post-hoc test, Pyr vs Int: $p_{vHPC} = 0.95$, $p_{dHPC} = 3.77e^{-9}$, $p_{dHPC\text{-}vHPC} = 3.77e^{-9}$, $p_{vHPC\text{-}dHPC} = 3.96e^{-9}$, Int vs Int: $p_{dHPC\text{-}vHPC} = 0.0004$, Pyr vs Pyr: $p_{dHPC\text{-}vHPC} = 3.77e_{-9}$; Number of Single-Units, dHPC: $N_{int} = 215$, $N_{pyr} = 856$, vHPC: $N_{int} = 83$, $N_{pyr} = 461$; Solid lines: mean).

https://doi.org/10.1038/s41593-026-02252-w

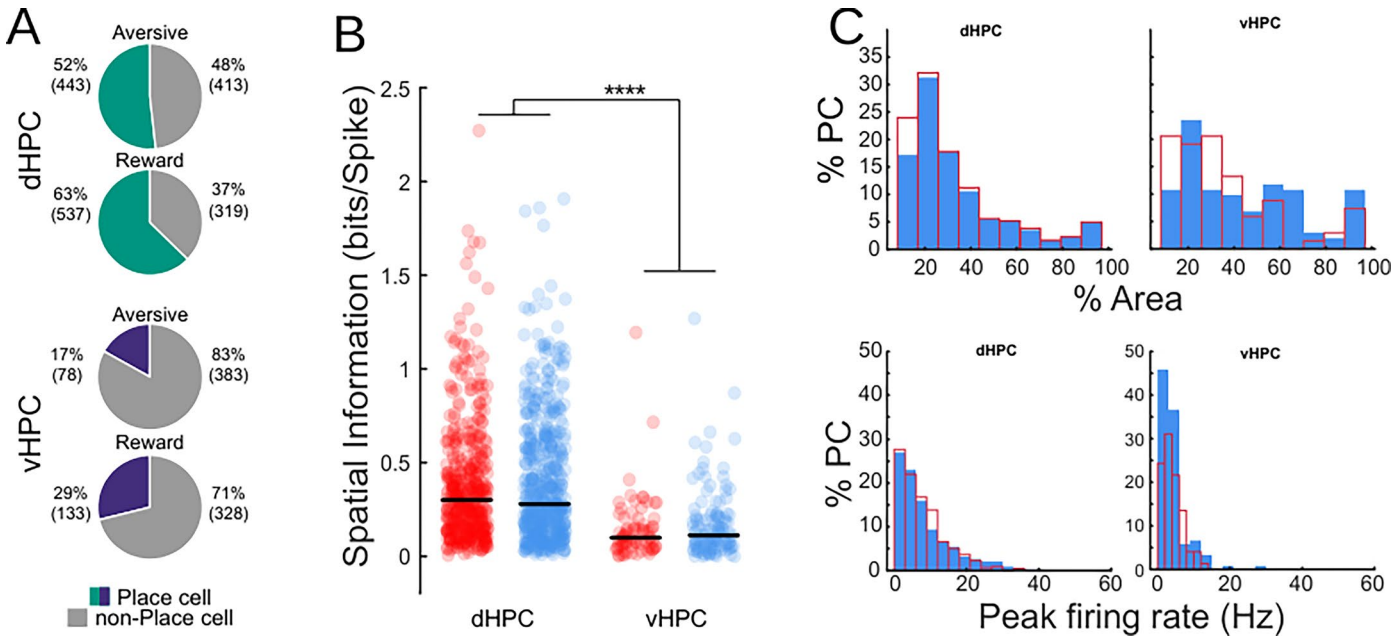

Extended Data Fig. 4 | Spatial Properties of dorsal and ventral place cells across conditions. A, Proportion of place cells among dorsal and ventral pyramidal neurons across emotional conditions. (Chi2, dHPC: ***p = 0.00001, vHPC: ***p = 0.00002). **B**, Spatial Information for dorsal (left) and ventral (right) place cells during aversive (red) and reward (blue) sessions (Two-way ANOVA. pinteraction=0.71, pcondition=0.48,****$p_{structure}$ = 2.2 e-16, Number of Place cells: N_{dHPC} = 656, N_{vHPC} = 193, Black lines: mean). **C**, Place cell characteristics across the dorsal-ventral hippocampal axis. Upper panel, Percentage of the area of the maze covered by the place-field in dHPC (left) and vHPC (right). Solid-bars histogram represent place-cells from reward run sessions, while empty-bar histogram represent those ones detected during aversive run sessions (One-sided two-sample Kolmogorov-Smirnov test, p_{dHPC} = 0.06, p_{vHPC} = 0.06, Number of Place cells: N_{dHPC} = 656, N_{vHPC} = 193). Lower panel, Peak firing rate for dorsal (right) and ventral (left) place-cells detected during the rewarded (blue) or aversive (red) condition (One-sided two-sample Kolmogorov-Smirnov test, dHPC: p = 0.11, vHPC: p = 0.78, Units Number: N_{dHPC} = 656, N_{vHPC} = 193).

https://doi.org/10.1038/s41593-026-02252-w

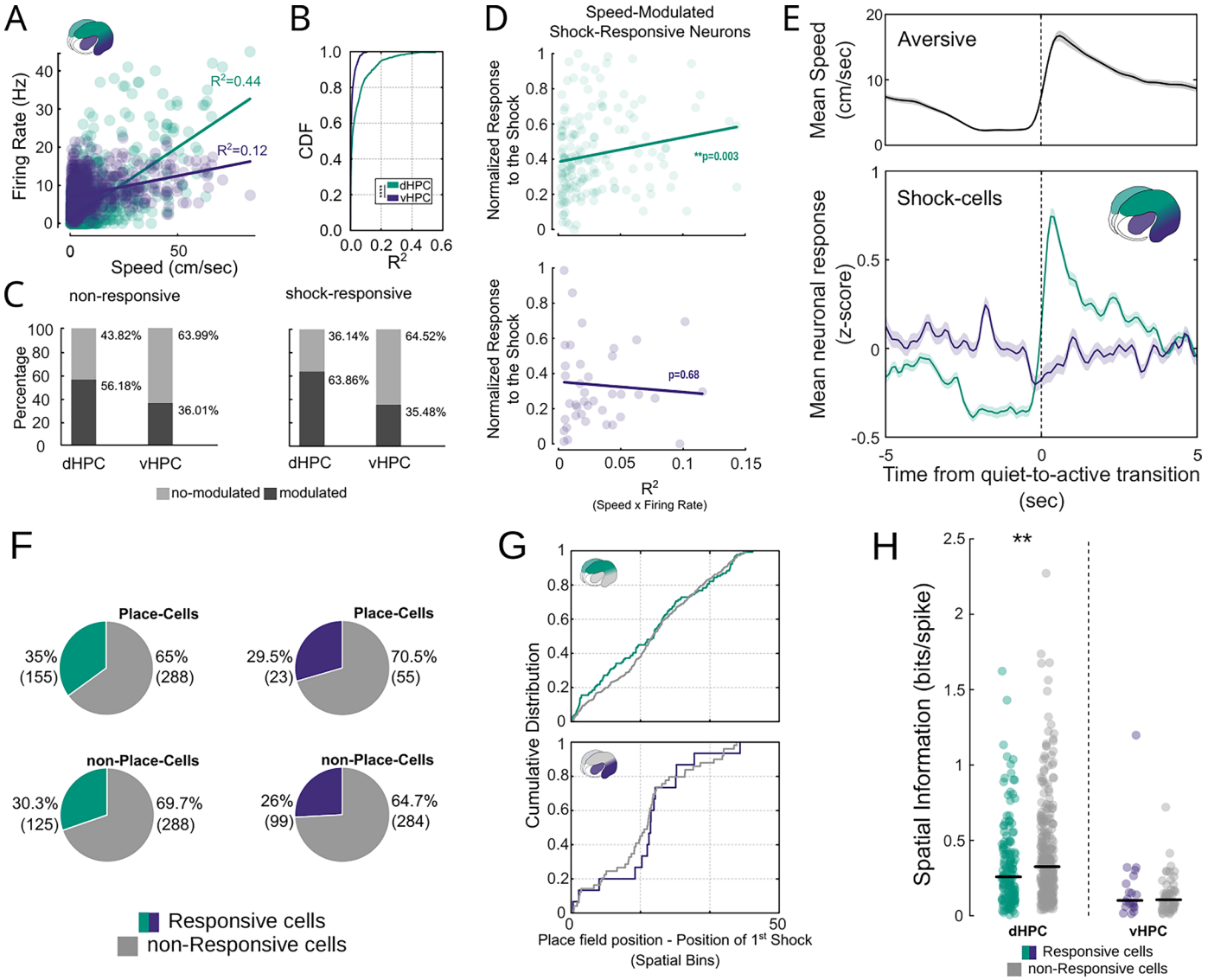

Extended Data Fig. 5 | Speed, shock and place-modulation of activity in aversive run. A, Linear correlation between the firing rate of 2 example putative pyramidal neurons and the animal's speed in the dHPC (green) and in the vHPC (purple). **B**, Cumulative Density Distribution of R-Square Linear Correlations for dHPC and vHPCl neurons (Two-sided Kolmogórov-Smirnov test, ****p = 4.61e-15). **C**, Percentage of speed-correlated and uncorrelated activity of shock-responsive and non-responsive neurons (non-responsive, Chi2, **p = 0.003; shock-responsive, Chi2, ****p = 0.00004). **D**, Linear correlation between the R-squared values of Speed-Neuronal activity in shock-responsive neurons (Upper panel: dHPC, $R^2 = 0.052$, p = 0.003, $N_{Sigle\text{-}Units} = 170$; Lower panel: vHPC, $R^2 = 0.004$, p = 0.68, $N_{Single\text{-}Units} = 40$). To ensure that the observed correlation in the dHPC was not due to the larger number of neurons, we subsampled the dHPC population 1,000 times to match the size of the vHPC population and performed linear regression. The R^2 value obtained from the entire population was not significantly different from the distribution generated by subsampling (Two-sided Kolmogórov-Smirnov test, p = 0.67). **E**, Activity of dorsal and ventral shock-responsive neurons during quiet-to-active transitions. Upper panel, Average speed across all transitions of aversive sessions($N_{Sessions}$=47, $N_{Transitions}$ = 45–108 per session). Lower panel, Normalized firing of dorsal (green) and ventral (purple) shock-responsive neurons. Dorsal responses followed speed dynamics, whereas ventral responses were not modulated by locomotion (Number of Shock-responsive cells: $N_{dHPC} = 285$, $N_{vHPC} = 124$). **F**, Percentage of shock-responsive (green: dHPC; purple: vHPC) and non-responsive (gray) cells, separated into place-cells and non–place-cells (Chi^2 test, Place vs. Non-Place: dHPC, $\chi^2 = 2.16$, p = 0.14; vHPC, $\chi^2 = 0.44$, p = 0.51). **G**, Cumulative distribution of the distance between the place-field position of shock-responsive place-cells (green/purple) and pure place-cells (gray) (Two-sided Kolmogorov–Smirnov test, $p_{dHPC} = 0.34$, $p_{vHPC} = 0.76$; Number of Place cells: dHPC, $N_{Responsive} = 155$, $N_{non\text{-}Responsive} = 288$, vHPC, $N_{Responsive} = 23$, $N_{non\text{-}Responsive} = 56$). **H**, Spatial information of shock-responsive vs. non-responsive place-cells (Two-sided Wilcoxon test, **$p_{dHPC} = 0.008$, $p_{vHPC} = 0.67$; Number of Place cells: dHPC, $N_{Responsive} = 155$, $N_{non\text{-}Responsive} = 288$, vHPC, $N_{Responsive} = 23$, $N_{non\text{-}Responsive} = 56$).

https://doi.org/10.1038/s41593-026-02252-w

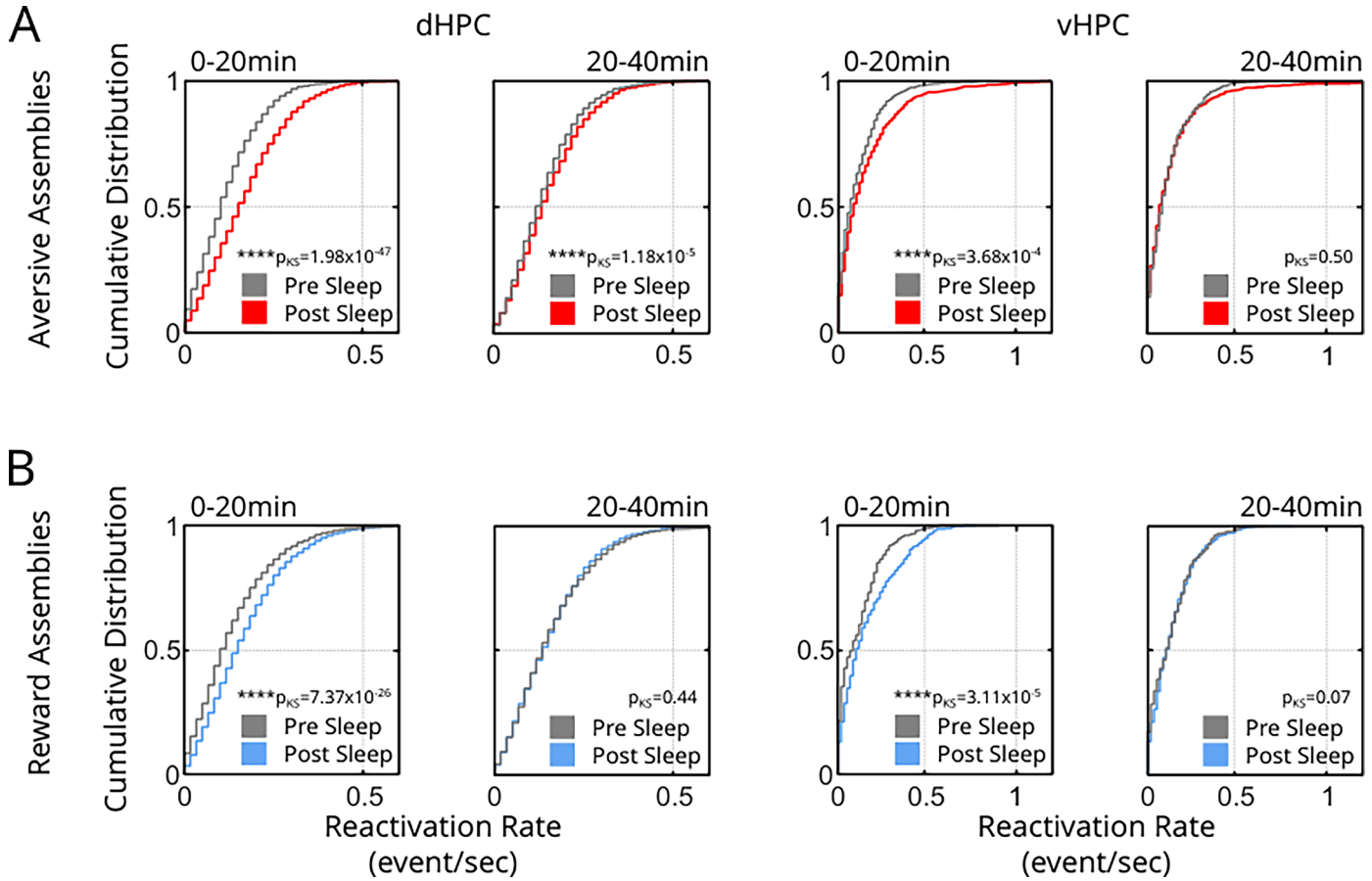

Extended Data Fig. 6 | Reactivation rate of dorsal and ventral assemblies. Cumulative distribution of assembly reactivation rate in 60 s bins during pre- and post-sleep sessions. The reactivation rate was calculated in 60-second bins aversive (**A**) and rewarded (**B**) assemblies' activity. In both: dHPC and vHPC assemblies, the reactivation rate was significantly higher at the beginning of the post-sleep session and progressively went back to pre-sleep levels at later time bins (One-sided Kolmogórov-Smirnov test, ****$p < 0.0001$; Number of Aversive assemblies: $N_{dHPC} = 131$, $N_{vHPC} = 37$; Number of Reward assemblies: $N_{dHPC} = 146$, $N_{vHPC} = 25$).

https://doi.org/10.1038/s41593-026-02252-w

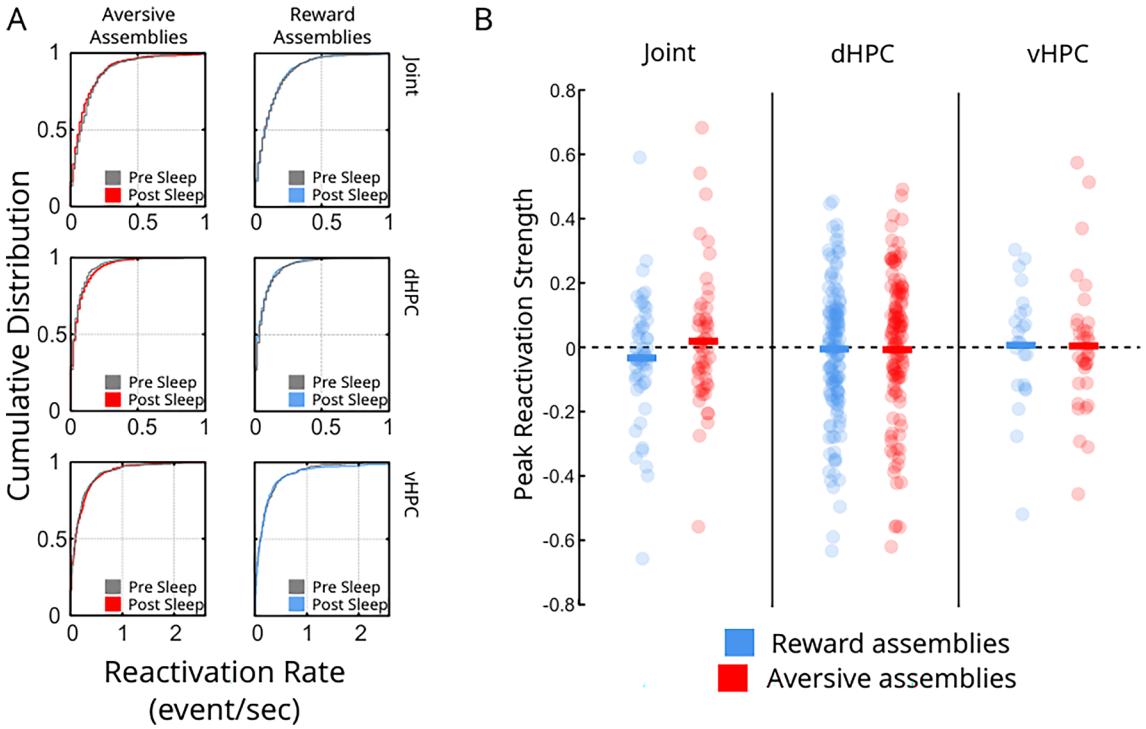

Extended Data Fig. 7 | Assembly reactivation during REM sleep. A, Cumulative distribution of aversive and rewarded assembly reactivation rate in 60 s bins during pre and post- NREM sleep for joint (top, dHPC (middle) and vHPC (bottom) assemblies (Two-sided Kolmogórov-Smirnov tests; Number of Assemblies: Joint: $N_{Reward} = 53$, $N_{Avesive} = 54$; dHPC: $N_{Reward} = 146$, $N_{Aversive} = 131$; vHPC: $N_{Reward} = 34$, $N_{Aversive} = 37$). **B**, Peak Reactivation Strength for all assembly types (Two-sided Mann-Whitney test, $p_{Joint} = 0.22$, $p_{dHPC} = 0.13$, $p_{vHPC} = 0.75$;; Number of Assemblies: Joint: $N_{Reward} = 53$, $N_{Avesive} = 54$; dHPC: $N_{Reward} = 146$, $N_{Aversive} = 131$; vHPC: $N_{Reward} = 34$, $N_{Aversive} = 37$). We also compared the Peak Reactivation Strength against zero to infer an increase of Reactivation Strength during Post-sleep compared to Pre-sleep (One-sided Mann-Whitney test against zero. Joint: $p_{Reward} = 0.86$, $p_{Aversive} = 0.45$; dHPC: $p_{Reward} = 0.47$, $p_{Aversive} = 0.07$; vHPC: $p_{Reward} = 0.21$, $p_{Aversive} = 0.50$; Number of Assemblies: Joint: $N_{Reward} = 53$, $N_{Avesive} = 54$; dHPC: $N_{Reward} = 146$, $N_{Aversive} = 131$; vHPC: $N_{Reward} = 34$, $N_{Aversive} = 37$; Solid lines: mean).

https://doi.org/10.1038/s41593-026-02252-w

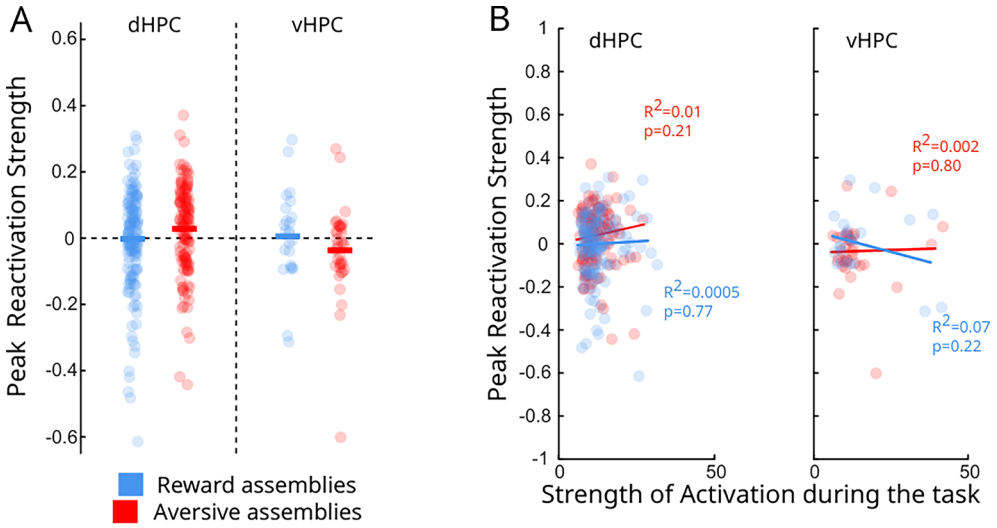

Extended Data Fig. 8 | Peak Reactivation Strength for aversive and rewarded dorsal and ventral assemblies. A, Peak Reactivation Strength for reward (blue) and aversive (red) assemblies with members coming only from the dorsal (dHPC) or ventral hippocampus (vHPC; One-sided Mann-Whitney test against zero; Number of Assemblies: dHPC, $N_{Aversive} = 131$, $N_{Reward} = 146$, $N_{Aversive} = 37$, $N_{Reward} = 34$). **B**, Correlation between the Peak Reactivation Strength and the Activation Strength during the task for dHPC (left panel) or vHPC (right panel) aversive and reward assemblies (Linear regression, Aversive assemblies, dHPC: $R^2 = 0.01$, $p_{slope} = 0.21$, $N_{Assemblies} = 131$; vHPC: $R^2 = 0.002$, $p_{slope} = 0.80$, $N_{Assemblies} = 37$; Reward assemblies, dHPC: $R^2 = 0.0005$, $p_{slope} = 0.77$, $N_{Assemblies} = 146$, vHPC: $R^2 = 0.07$, $p_{slope} = 0.22$, $N_{Assemblies} = 24$).

https://doi.org/10.1038/s41593-026-02252-w

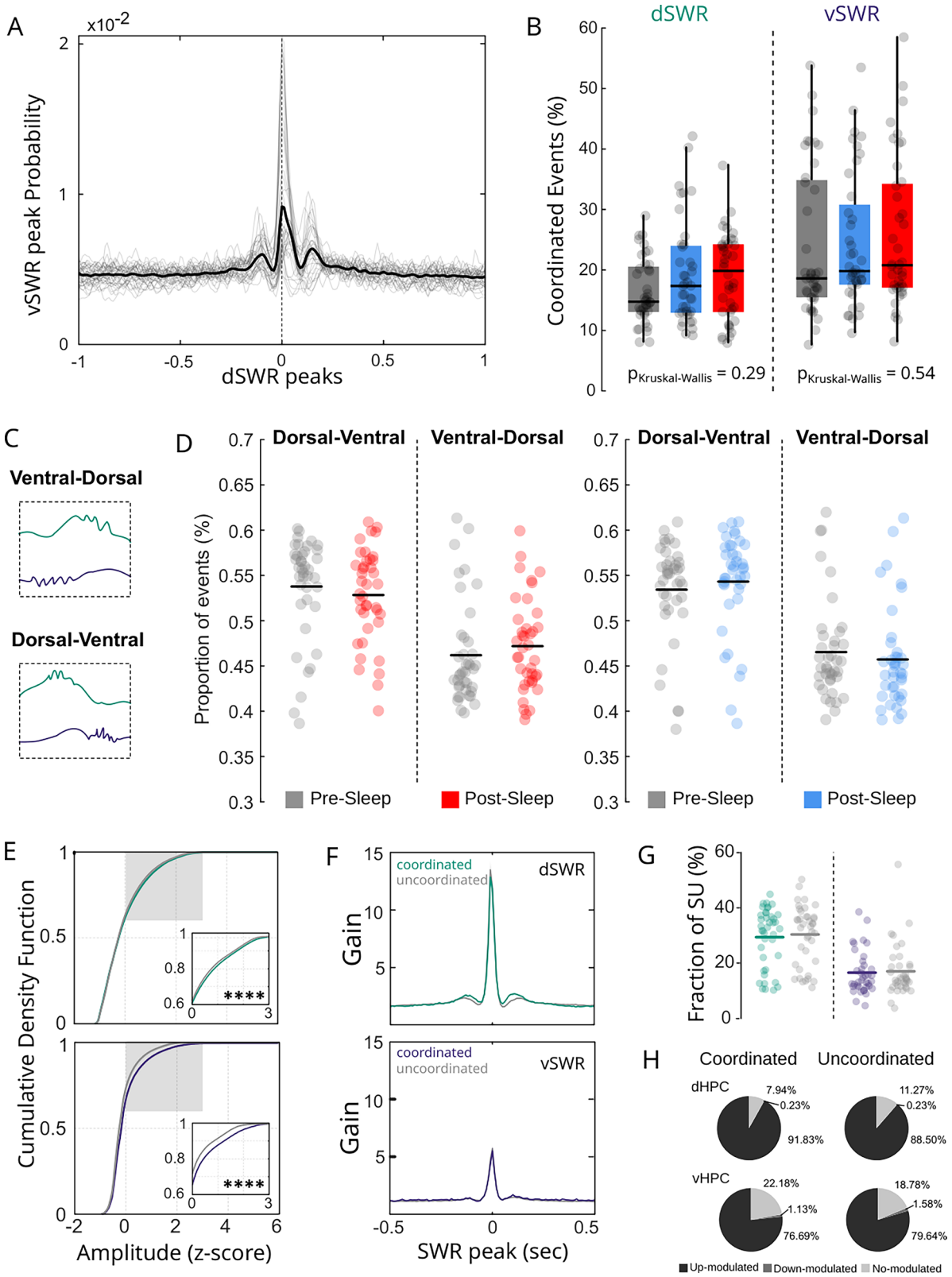

Extended Data Fig. 9 | See next page for caption.

https://doi.org/10.1038/s41593-026-02252-w

Extended Data Fig. 9 | Characterization of dorsal-ventral ripple coordination across conditions. A, Peri-event density of ventral ripple peak density centered on dorsal ripple peaks for individual sessions (grey) and averaged across all sessions (black) showing the co-occurrence of dSWRs and vSWRs within a +/− 100 ms window (dashed lines). **B**, Percentage of coordinated events across sleep sessions (Kruskal-Wallis test, dSWRs: p = 0.29; vSWRs: p = 0.54, whiskers extend to minimal and maximal data points, box edges are 25th and 75th percentile, line represents median, $N_{sessions}$ = 40). **C-D** Percentage of ventral- and dorsal-leading events were segregated across pre- (in gray) and post-sleep (aversive in red, reward in light blue) sessions (Two-sided paired Wilcoxon test; aversive, p = 0.19; reward, p = 0.27; $N_{sessions}$ = 40). **E**, Cumulative density function of ripple peak amplitude for coordinated (green/purple) and uncoordinated ripples (grey). (Two-sided Kolmogórov-Smirnov test, dSWRs, ****$p = 5.58e^{-24}$; vSWRs, ****$p = 5.58e^{-24}$). **F**, Peri-event activity gain for pyr single units for coordinated and uncoordinated dorsal (upper) and ventral (lower) ripples (Two-sided paired Wilcoxon test; Solid lines: mean; shaded areas: ±SEM). **G**, Average fraction of single-units recruited during coordinated (in color) and uncoordinated (grey) ripples (Two-sided paired Wilcoxon test, p_{dHPC} = 0.18, p_{vHPC} = 0.95, $N_{sessions}$ = 40, Solid lines: mean). **H**, Percentages of modulated vs. non-modulated neurons for each ripple type (Chi^2 across structures: X^2 = 6.35, p = 0.1).

https://doi.org/10.1038/s41593-026-02252-w

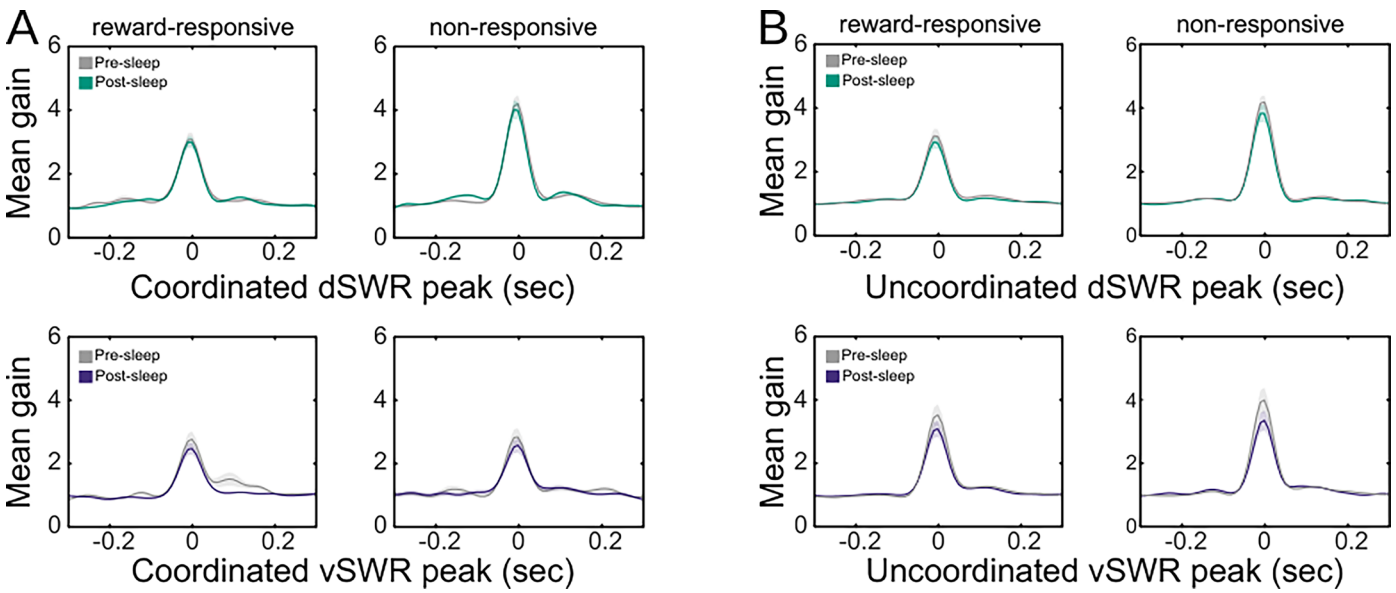

Extended Data Fig. 10 | Reward-responsive Members from joint assemblies do not change their response during ripples. Reward-responsive cells response locked to coordinated and uncoordinated ripples. **A**, Average gain in firing rate around coordinated ripple onset during NREM sleep preceding (grey) and following (green/purple) reward runs (One-sided Mann-Whitney test. dHPC, $p_{responsive} = 0.53$, $p_{non\text{-}responsive} = 0.80$). (vHPC, $p_{Responsive} = 0.44$, pnon-responsive = 0.92). **B**, Average gain in firing rate around uncoordinated ripple onset during NREM sleep preceding (grey) and following (green/purple) reward runs (One-sided Mann-Whitney test; dHPC, $p_{Responsive} = 0.72$, $p_{non\text{-}Responsive} = 0.87$, $N_{Single\text{-}Units} = 62$; vHPC, $p_{Responsive} = 0.43$, $p_{non\text{-}Responsive} = 0.14$, $N_{Single\text{-}Units} = 54$; Solid lines: mean; shaded areas: ±SEM).

nature portfolio

Corresponding author(s): Gabrielle Girardeau

Last updated by author(s): Feb 2, 2026

Reporting Summary

Nature Portfolio wishes to improve the reproducibility of the work that we publish. This form provides structure for consistency and transparency in reporting. For further information on Nature Portfolio policies, see our Editorial Policies and the Editorial Policy Checklist.

Statistics

For all statistical analyses, confirm that the following items are present in the figure legend, table legend, main text, or Methods section.

n/a	Confirmed	
☐	☒	The exact sample size (*n*) for each experimental group/condition, given as a discrete number and unit of measurement
☐	☐	A statement on whether measurements were taken from distinct samples or whether the same sample was measured repeatedly
☐	☒	The statistical test(s) used AND whether they are one- or two-sided *Only common tests should be described solely by name; describe more complex techniques in the Methods section.*
☐	☒	A description of all covariates tested
☐	☒	A description of any assumptions or corrections, such as tests of normality and adjustment for multiple comparisons
☐	☒	A full description of the statistical parameters including central tendency (e.g. means) or other basic estimates (e.g. regression coefficient) AND variation (e.g. standard deviation) or associated estimates of uncertainty (e.g. confidence intervals)
☐	☒	For null hypothesis testing, the test statistic (e.g. *F*, *t*, *r*) with confidence intervals, effect sizes, degrees of freedom and *P* value noted *Give P values as exact values whenever suitable.*
☒	☐	For Bayesian analysis, information on the choice of priors and Markov chain Monte Carlo settings
☒	☐	For hierarchical and complex designs, identification of the appropriate level for tests and full reporting of outcomes
☒	☐	Estimates of effect sizes (e.g. Cohen's *d*, Pearson's *r*), indicating how they were calculated

Our web collection on statistics for biologists contains articles on many of the points above.

Software and code

Policy information about availability of computer code

Data collection	Intan RHD recording system software, 64 and 32-channels RHD headstage, Basler camera (ace Basler 106754)
Data analysis	Commercial software: MATLAB (MathWorks) version R2020a Open-source code (for MATLAB): Kilosort version 2.5 (https://github.com/MouseLand/Kilosort) FMAtoolbox(https://github.com/michael-zugaro/FMAToolbox). All codes used to generate the figures are available on the Girardeau Lab github repository (https://github.com/GirardeauLab/Morici_2026).

For manuscripts utilizing custom algorithms or software that are central to the research but not yet described in published literature, software must be made available to editors and reviewers. We strongly encourage code deposition in a community repository (e.g. GitHub). See the Nature Portfolio guidelines for submitting code & software for further information.

Data

Policy information about availability of data

All manuscripts must include a data availability statement. This statement should provide the following information, where applicable:

- Accession codes, unique identifiers, or web links for publicly available datasets
- A description of any restrictions on data availability
- For clinical datasets or third party data, please ensure that the statement adheres to our policy

The dataset generated during the current study will be available upon reasonable request to Corresponding and First Author.

Research involving human participants, their data, or biological material

Policy information about studies with human participants or human data. See also policy information about sex, gender (identity/presentation), and sexual orientation and race, ethnicity and racism.

Reporting on sex and gender	N/A
Reporting on race, ethnicity, or other socially relevant groupings	N/A
Population characteristics	N/A
Recruitment	N/A
Ethics oversight	N/A

Note that full information on the approval of the study protocol must also be provided in the manuscript.

Field-specific reporting

Please select the one below that is the best fit for your research. If you are not sure, read the appropriate sections before making your selection.

☒ Life sciences ☐ Behavioural & social sciences ☐ Ecological, evolutionary & environmental sciences

For a reference copy of the document with all sections, see nature.com/documents/nr-reporting-summary-flat.pdf

Life sciences study design

All studies must disclose on these points even when the disclosure is negative.

Sample size	We analyzed a dataset of 1615 units, 1071 from dorsal hippocampus and 544 from the ventral hippocampus of 6 rats. The activity of each unit was recorded for ~7 hours. No power analysis was used to pre-determine the sample size. The number of animals and neurons are typical for studies in this research field in rodents.
Data exclusions	Sessions including less than 3 neurons in the dorsal or ventral hippocampus were excluded for the detection of assemblies (see methods). We excluded the data from the dorsal hippocampal electrode of the rat 126 since electrode did not reach the pyramidal layer.
Replication	The experiments were conjointly conducted by 2 experimenters (JMF, ILP). Data analysis were cross-checked by two co-authors (JFM, AS).
Randomization	Across days, the Aversive and Reward runs were presented in a pseudo-randomized order, ensuring both Aversive-Reward and Reward-Aversive combinations occurred roughly equally throughout the experiment.
Blinding	The study did not include experimental subject groups, so experimenter blinding was not applicable and was not implemented.

Reporting for specific materials, systems and methods

We require information from authors about some types of materials, experimental systems and methods used in many studies. Here, indicate whether each material, system or method listed is relevant to your study. If you are not sure if a list item applies to your research, read the appropriate section before selecting a response.

Materials & experimental systems

n/a	Involved in the study
☒	☐ Antibodies
☒	☐ Eukaryotic cell lines
☒	☐ Palaeontology and archaeology
☐	☒ Animals and other organisms
☒	☐ Clinical data
☒	☐ Dual use research of concern
☒	☐ Plants

Methods

n/a	Involved in the study
☒	☐ ChIP-seq
☒	☐ Flow cytometry
☒	☐ MRI-based neuroimaging

Animals and other research organisms

Policy information about studies involving animals; ARRIVE guidelines recommended for reporting animal research, and Sex and Gender in Research

Laboratory animals	Long Evan rats, female (300g/3 months-old at the time of the surgery).
Wild animals	This study did not involve wild animals.
Reporting on sex	Female rats were included in this study. Sex-based analyses were not performed.
Field-collected samples	This study did not involve samples collected from the field.
Ethics oversight	Protocols approved by the French Committee of Ethics (APAFIS #35991-2022031810445522 v3)

Note that full information on the approval of the study protocol must also be provided in the manuscript.

Plants

Seed stocks	N/A
Novel plant genotypes	N/A
Authentication	N/A